Hindawi Publishing Corporation
International Journal of Geophysics
Volume 2013, Article ID 804216, 26 pages
http://dx.doi.org/10.1155/2013/804216

Research Article

Identifying Buried Segments of Active Faults in the Northern Rio Grande Rift Using Aeromagnetic, LiDAR, and Gravity Data, South-Central Colorado, USA

V. J. S. Grauch[1] and C. A. Ruleman[2]

[1] *U. S. Geological Survey, MS 964, Federal Center, Denver, CO 80225, USA*
[2] *U. S. Geological Survey, MS 980, Federal Center, Denver, CO 80225, USA*

Correspondence should be addressed to V. J. S. Grauch; tien@usgs.gov

Received 1 November 2012; Revised 15 February 2013; Accepted 4 March 2013

Academic Editor: Luciano Scarfi

Combined interpretation of aeromagnetic and LiDAR data builds on the strength of the aeromagnetic method to locate normal faults with significant offset under cover and the strength of LiDAR interpretation to identify the age and sense of motion of faults. Each data set helps resolve ambiguities in interpreting the other. In addition, gravity data can be used to infer the sense of motion for totally buried faults inferred solely from aeromagnetic data. Combined interpretation to identify active faults at the northern end of the San Luis Basin of the northern Rio Grande rift has confirmed general aspects of previous geologic mapping but has also provided significant improvements. The interpretation revises and extends mapped fault traces, confirms tectonic versus fluvial origins of steep stream banks, and gains additional information on the nature of active and potentially active partially and totally buried faults. Detailed morphology of surfaces mapped from the LiDAR data helps constrain ages of the faults that displace the deposits. The aeromagnetic data provide additional information about their extents in between discontinuous scarps and suggest that several totally buried, potentially active faults are present on both sides of the valley.

1. Introduction

The combination of aeromagnetic methods and LiDAR (Light Detection And Ranging) mapping has proved useful for identifying active faults in dynamically deforming, compressional terranes in the Pacific Northwest region of USA [1, 2]. Linear aeromagnetic anomalies and gradients corresponding to thrust and tear faults are associated with fault scarps on the ground, located by airborne LiDAR surveys. The scarps are otherwise difficult to identify in the highly populated areas and under widespread, dense vegetative cover.

Recent acquisition of aeromagnetic and airborne LiDAR data over the northern Rio Grande rift in the southwestern USA has afforded the opportunity to test these methods in a less active, extensional basin in a semiarid environment. Farther south, in the central Rio Grande rift, aeromagnetic methods have proved useful for mapping intrasedimentary faults under cover [3], but age of activity cannot be determined from aeromagnetic data alone. Although dense vegetation and population are not as widespread as in the Pacific Northwest, active fault scarps can still be difficult to identify because of widespread eolian cover and dynamic weathering. Thus, combined analysis of high-resolution aeromagnetic data and LiDAR images builds on the strength of the aeromagnetic method to locate normal faults with significant offset under cover and the strength of LiDAR interpretation to identify subtle topographic scarps. Moreover, combining these methods can resolve ambiguities in locating the surface projections of buried faults from aeromagnetic data and in distinguishing tectonic versus fluvial origins of topographic scarps recognized from LiDAR data. Once active faults are identified, information from geologic mapping, trenching, and gravity and seismic-reflection data can provide additional constraints on age, recurrence history, amount of offset, and sense of displacement.

Herein we present a case history of combined interpretation of the recently acquired high-resolution aeromagnetic and LiDAR data from the very northern part of the San Luis Basin, one of the largest of the series of alluvial basins that comprise the northern part of the Rio Grande rift (Figure 1 inset). Although only a few historic earthquakes have been recorded in the northern Rio Grande rift, the rift is still considered active. The potential for seismic hazard is based on evidence of large-magnitude earthquakes (M 6.8–7.1) with recurrence intervals of 10–140 ka [4–10]. Thus, active fault scarps may not be easily recognized because they can be quiescent for long periods of time, subject to erosion. We present several examples that elucidate the strengths and limitations of combining the LiDAR and aeromagnetic data to identify and characterize active faults at basin margins and within the interior of the basin.

2. Geologic and Tectonic Setting

Our study area is located in the northern part of the San Luis Valley, south-central Colorado, within the San Luis Basin of the northern Rio Grande rift (Figure 1). The northwest-elongated valley is bounded on the east by the steep slopes of the Sangre de Cristo Mountains and on the west by low hills at the northeastern edge of the San Juan volcanic field (Figure 1 inset).

The northern San Luis Basin, like other parts of the Rio Grande rift, has been the site of multiple tectonic events that each left an imprint on the geology and underlying structure [11]. Geophysical interpretation of rift structure commonly requires unraveling the similar-looking expressions of older tectonic features from those of the rift. The first of three major prerift events of importance to the region is the Mississippian-Pennsylvanian (Carboniferous) Ancestral Rocky Mountain orogeny. This tectonic event left a regional, north-south uplift that now underlies the central portion of the San Luis Basin. The uplift is evidenced from gravity data, seismic-reflection sections, and deep drilling to the south of the study area [12]. Eventual denudation of the uplift shed detritus into an adjacent basin to the east, accumulating as much as 4 km of clastic sedimentary rocks [13]. These rocks, along with underlying Early Paleozoic marine carbonates and sandstones, unconformably overlie Proterozoic crystalline basement and are exposed at the margins of the valley (Figure 1).

During Late Cretaceous to Eocene, thrust faulting and folding during the Laramide orogeny developed large reverse and low-angle faults, accompanied by strike-slip faulting. The thrusting transported Late Paleozoic rocks kilometers to the east and northeast into deformed and stacked thrust packages that lie mostly within the western front of the Sangre de Cristo Mountains today [14]. Toward the end of the Laramide orogeny, uplifts were again eroded, shedding detritus to the west into a depression now located in the subsurface on the western side of the San Luis Basin [15].

From Late Eocene to Late Oligocene, extensive lava flows and ash-flow eruptions originated from the San Juan volcanic field to the south and west of the study area (inset on Figure 1). The 33.2-Ma Bonanza caldera lies at the western side of the study area [16, 17]. Tertiary volcanic rocks exposed in the northern part of the study area mostly represent Bonanza tuff and precaldera andesite.

Basin subsidence related to Rio Grande rifting overlapped the waning of primarily intermediate to silicic volcanic activity of the San Juan and related volcanic fields in Late Oligocene and the onset of mafic volcanism in the southern San Luis Basin [18]. Subsidence was most active during Miocene time and has diminished since the beginning of the Pliocene [19]. From recent GPS studies, deformation appears to be evenly distributed across the rift instead of being focused at the rift margins [20].

The northern half of the San Luis Basin, in the northern Rio Grande rift, forms an asymmetric, east-tilted half graben, with 6-7 km of total displacement [12, 15]. The Sangre de Cristo fault zone (Figure 1) is commonly cited as the eastern margin of this half graben, extending in length from 79 to 104 km, depending on whether it is defined by orientations of the range front, slip rates, or geomorphic expression [5, 7, 10, 21]. Sediments that filled the Miocene-Pliocene basins consist of poorly consolidated sands, silts, and gravels of the Santa Fe Group. Deposits of this age are found at high elevations to the east and north of the study area, suggesting that early rifting had a different orientation and locus of deposition in this region before Pliocene time ([22] and references therein). Our study area is located where the basin narrows dramatically (Figure 1 inset) and marks the southern end of a poorly understood zone of transition from the strongly east-tilted half-graben of the central San Luis Basin on the south, to a strongly west-tilted half-graben in the next basin to the north [23].

Several periods of Pleistocene glaciation in the region are recorded by deposits of stream and fan alluvium, till, and outwash, which are mainly preserved near the mountain fronts. The relative ages of these deposits are determined from geomorphology and degree of weathering and soil development. From the youngest to the oldest, these deposits are Qfy, Qfi, and Qfo (Figure 1) and are associated with Pinedale, Bull Lake, and pre-Bull Lake glaciations, respectively. Based on regional correlations from previous and recent work, the glaciations in this area correspond to the following age ranges: Pinedale (12–30 ka), Bull Lake (about 120–170 ka), and pre-Bull Lake (170–640 ka) [21, 24–31]. The most recent (<10 ka) deposits in the area are Holocene stream and fan alluvium deposits, unit Qh (Figure 1).

Precipitous, faceted spurs aligned along the range front mark the steeply west-dipping northern Sangre de Cristo fault zone on the east side of the valley (Figure 1). The northwest-trending Villa Grove fault zone, composed of multiple, mainly southwest-facing scarps developed in fan deposits, diverges from the northern Sangre de Cristo fault zone near the southeastern corner of the study area. The zone extends northwestward across the valley for about 10 km, in apparent connection with easterly facing scarps on the west side of the valley near Villa Grove (Figure 1; [10]). Kellogg [32] suggests that much of Rio Grande rift structure is inherited from preexisting Laramide thrust fault geometry, but with reversed sense of motion.

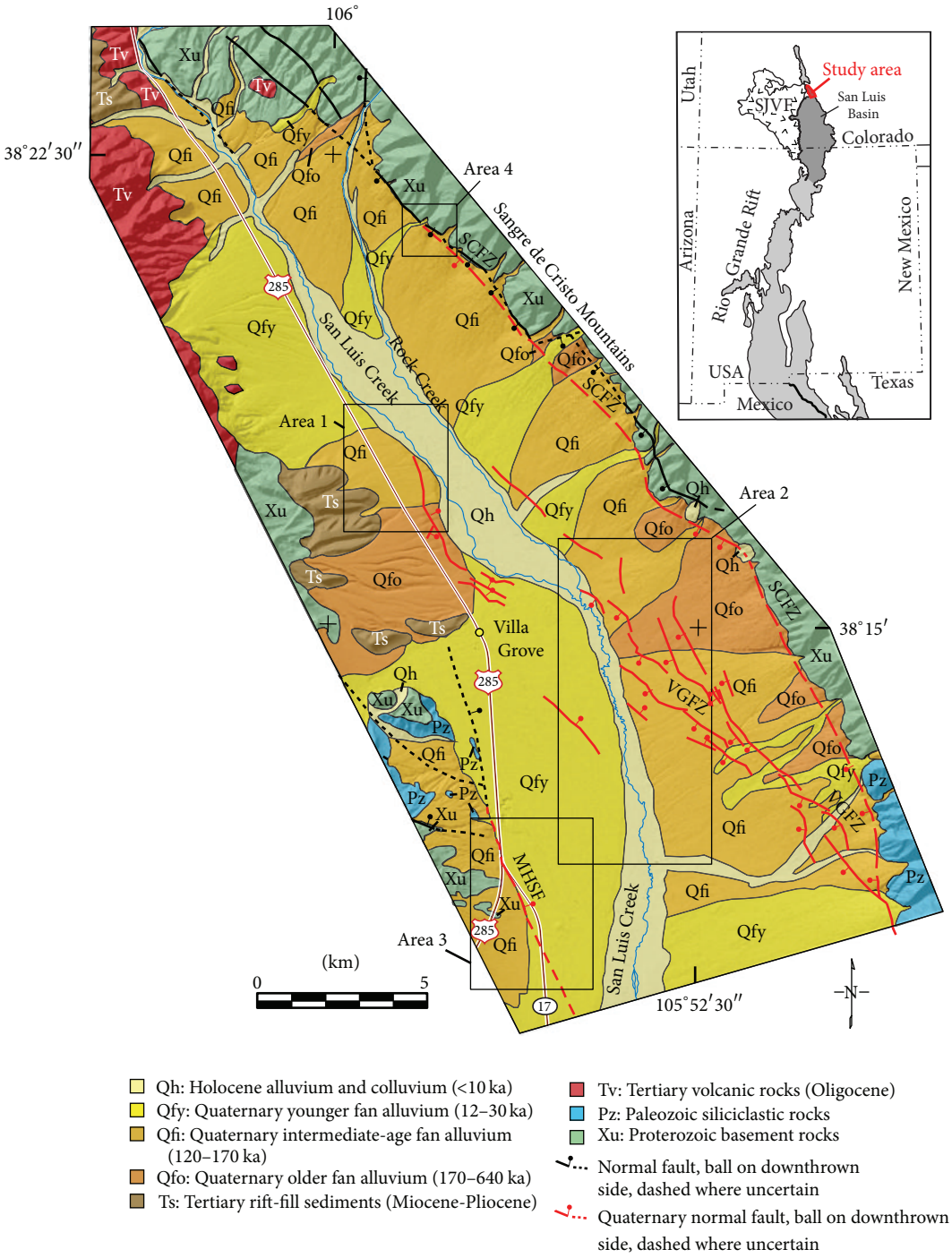

Figure 1: Geology of the northern San Luis Valley area from published sources (see text). Modifications and additions to these mapped Quaternary (active) faults and general surficial geology are presented in this study (Figure 15). Underlay of shaded-relief terrain is a graphically smoothed, NW-illuminated hillshade derived from the LiDAR data (Figure 3). MHSF: Mineral Hot Springs fault, SCFZ: Sangre de Cristo fault zone, and VGFZ: Villa Grove fault zone. Boxes locate example Areas 1–4. Inset shows the location of the study area within the San Luis Basin and Rio Grande rift (basins are shaded). SJVF: San Juan volcanic field.

All faults in the study area that displace Quaternary deposits (red lines on Figure 1) are considered active. The potential for seismic hazard is based on evidence of large-magnitude earthquakes (M 6.8–7.1) with recurrence intervals of 10–140 ka [4–10].

3. Data Sources

3.1. Previous Geologic Mapping. The geologic map shown in Figure 1 is generalized from several compilations by others. Geology shown east of 106° longitude and north of 38°22′30″

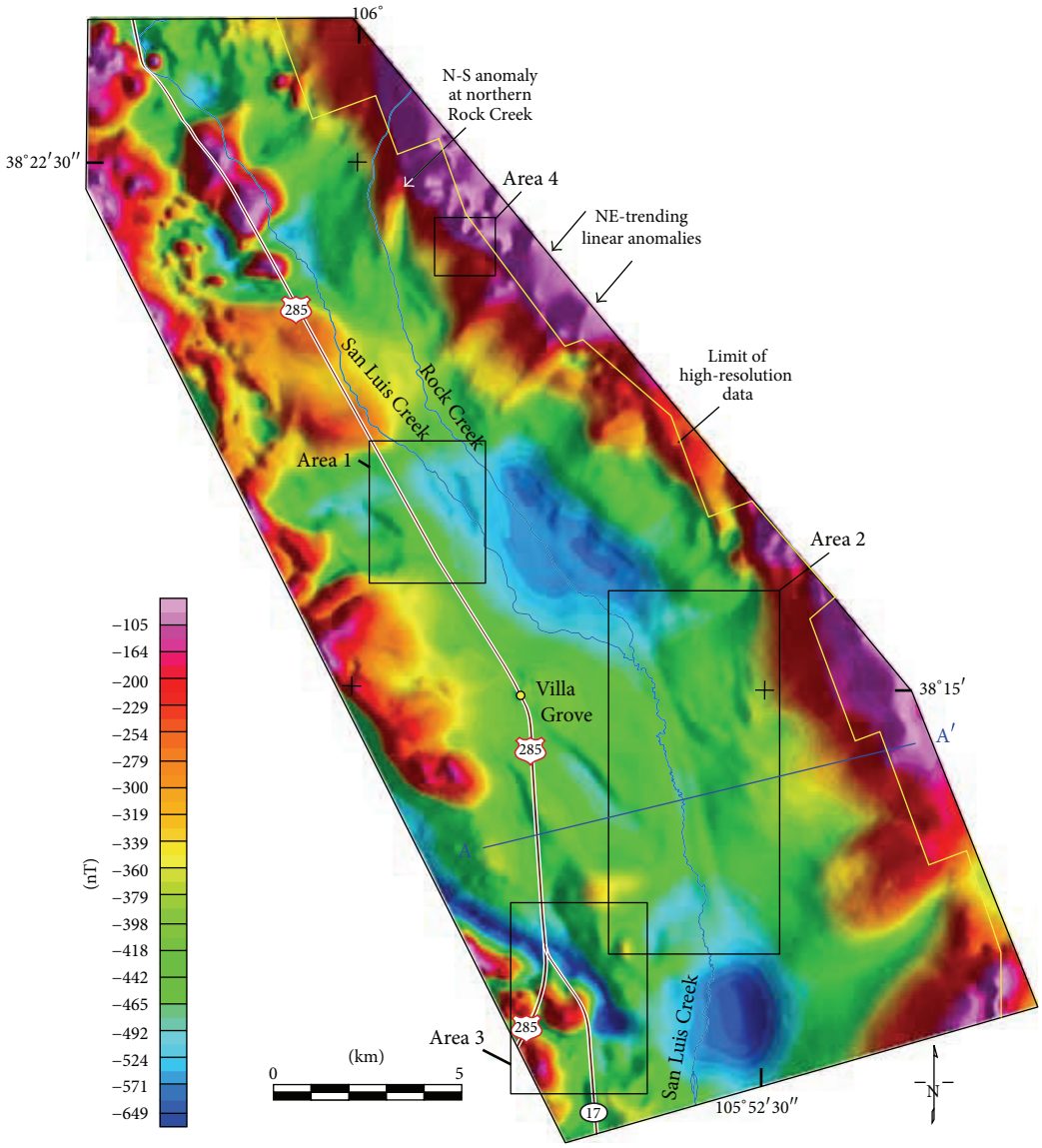

Figure 2: Reduced-to-pole (RTP) aeromagnetic data for the study area. Illuminated from the east. Data from the modern high-resolution aeromagnetic survey was merged with older, analog data west of the survey boundary (yellow line), described in text. Boxes locate example Areas 1–4. Model for A-A′ is shown in Figure 16.

latitude was generalized from a geologic compilation for central Colorado undergoing review within the U.S. Geological Survey (USGS) as of 2012. Terry Klein (USGS, retired) led the compilation for this area, which he assembled and edited from previous publications [24, 33–36]. The geology for the remaining part of our study area was generalized from compilations by Colman et al. [24] and Kappa and Wallace [37]. Documentation of ages listed for the surficial units is described in Section 2.

3.2. Aeromagnetic Data. High-resolution aeromagnetic data covering most of the study area (Figure 2) are from a survey flown on contract to the USGS by EON Geosciences, Inc., in October, 2011, over a much larger area of the northern San Luis Basin and regions to the north. The survey was flown by helicopter along lines oriented east northeast (70° east of north) and 150 m apart. Over most of the survey area, the pilot followed a preplanned, smooth flight surface that averaged 100 m above ground over the whole study area but reached as much as 300 m over the mountain front. Survey coverage in the mountainous areas was limited due to regulations restricting low flying over the Sangre de Cristo Wilderness Area. After standard data processing and removal of the 2010 reference field for the Earth for the date of the survey [38], flight-line data were gridded onto a 50 m grid and analytically continued to a more consistent surface 100 m above the ground.

Data for the missing areas over the mountains were obtained from project 4068 from a database developed for North America [39]. The survey for this project was originally

flown in 1981 along northeast-southwest lines spaced about 400 m apart at 300 m above ground. Due to numerous problems discovered with the original location data for this survey, the line data were extensively decimated before gridding and no continuation was attempted. Data problems that remain commonly produce linear artifacts oriented along the direction of the flight lines. Nevertheless, the data are useful for providing a more comprehensive picture of the aeromagnetic data for our study area. The data were digitally merged with the high-resolution grid by smoothly blending the overlapping areas.

A standard reduction-to-pole operator was applied to the continued, merged magnetic grid, using a declination and inclination of the presentday Earth's field of 9.2° and 65°, respectively (Figure 2). The underlying assumption in using reduced-to-pole data for interpretation is that magnetizations in the study area are generally collinear with the Earth's field. This assumption is valid for the rift sediments and Paleozoic sedimentary units, which do not carry much remanence. It is likely valid for the Tertiary volcanic rocks and Proterozoic basement rocks that produce large-amplitude anomalies. The Tertiary volcanic rocks formed when Earth field directions were approximately parallel or opposite to those of today. The magnetizations of Proterozoic rocks are likely dominated by the induced component, based on the results of a study just north of our area [40].

3.3. LiDAR Data. LiDAR (Light Detection and Ranging) data were acquired in 2010, using an airborne-laser nominal pulse spacing of 1 meter. Supplemented with ground control positioning, the final dataset has a vertical and horizontal RMSE (root mean square error) of <12.5 cm and <10 cm, respectively. The final full-point cloud was provided as bare-earth coded points in order to generate bare-earth surface raster DEM (Digital Elevation Model) data with a cell size of 1 meter. The required vertical accuracy for the bare-earth DEM was 24.5 cm at a 95% confidence level, but the tested accuracy was 10 cm. The "bare-earth" terrain model was converted to shaded-relief images illuminated from NE, SE, NW, and SW for interpretations used herein (Ted Brandt, USGS, written communication, 2012). The hillshade with NW illumination, decimated for viewing at page size is shown in Figure 3.

3.4. Gravity Data. Gravity data were prepared by Benjamin Drenth (USGS) from principal facts extracted from a gravity-data web portal for the United States [41], supplemented by new data acquired during 2012. Figure 4 shows the irregular data coverage for the study area. The data were checked for consistency, then processed following standard techniques, using a reduction density of 2,670 kg/m^3 for Bouguer and terrain corrections. After gridding at a 1 km interval, a regional field was removed to focus on anomalies of the upper crust. The regional field was computed from an isostatic model using parameters developed by Heywood [42]. The resulting isostatic residual gravity grid is shown in Figure 4.

Measurements of bulk density in nearby areas of the Rio Grande rift indicate that contrasts on the order of 400 kg/m^3 arise from the juxtaposition of bedrock against poorly consolidated Tertiary and Quaternary deposits [40, 43]. Lesser density contrasts of 100–210 kg/m^3 arise from the juxtaposition of Tertiary volcanic rocks or Paleozoic sedimentary rocks against Proterozoic rocks. Significant density contrasts are not typically observed between different facies of the sediments themselves. Thus, gravity lows in the study area are expected to be primarily a function of variations in the overall thickness of rift sediments, implying that the gravity lows generally reflect the shapes of the rift basin.

3.5. Seismic-Reflection Data. Seismic-reflection data were collected along several lines across the southern part of the study area in the 1970s [44, 45] but have limited use for our study. The original data are no longer available; only poor-quality figures of the sections remain. Reflections within the first 0.2 seconds of two-way travel time are insufficiently displayed in the figures to examine shallow rift faults. Davis and Stoughton [45] suggest that ~1.3 km thick sections of complexly folded and faulted Paleozoic sedimentary rocks underlie a fairly shallow rift basin (<500 m thick) underneath the valley. However, geologic interpretations of the sections are ambiguous because no well data are available for comparison.

4. Methods

4.1. Identifying Faults from Aeromagnetic Data. Grauch and Hudson [3] have demonstrated the utility and challenges of using high-resolution aeromagnetic data to interpret shallow normal faults for the central Rio Grande rift. Widespread, partially concealed and totally buried faults that offset Tertiary and younger rift sediments within basins of the central Rio Grande rift are expressed as numerous subtle, northerly trending, linear anomalies. Using field observations, physical property measurements, and magnetic modeling, they found that the aeromagnetic anomalies are caused by the tectonic juxtaposition of magnetically differing strata rather than by chemical processes acting at the fault zone, as widely speculated in earlier work from other areas. Field evidence for chemical processes that produce or destroy magnetic minerals in sufficient volume to create aeromagnetic anomalies from rift sediments is lacking in our study area as well.

Using commonly observed magnetic properties for sediments in the central Rio Grande rift [46], Grauch and Hudson [3] estimate that faults near the surface require at least 30 m of throw to produce the observable aeromagnetic anomalies, indicating that faults with aeromagnetic expression likely have significant vertical displacement. However, not all faults with significant vertical displacement juxtapose layers of differing magnetic properties, even along strike, so that aeromagnetic data may not reveal all faults or the total lengths of individual faults. Moreover, age and sense of motion of aeromagnetically expressed faults cannot be determined without independent information.

A useful approach to mapping the locations of faults involves the computation of the horizontal gradient magnitude (HGM) of the reduced-to-pole aeromagnetic data [3]. The utility and difficulties with the approach are illustrated in four end-member models that represent where magnetic contrasts are developed at simple offsets of layered strata at normal faults (Figure 5). Although developed for faults that offset

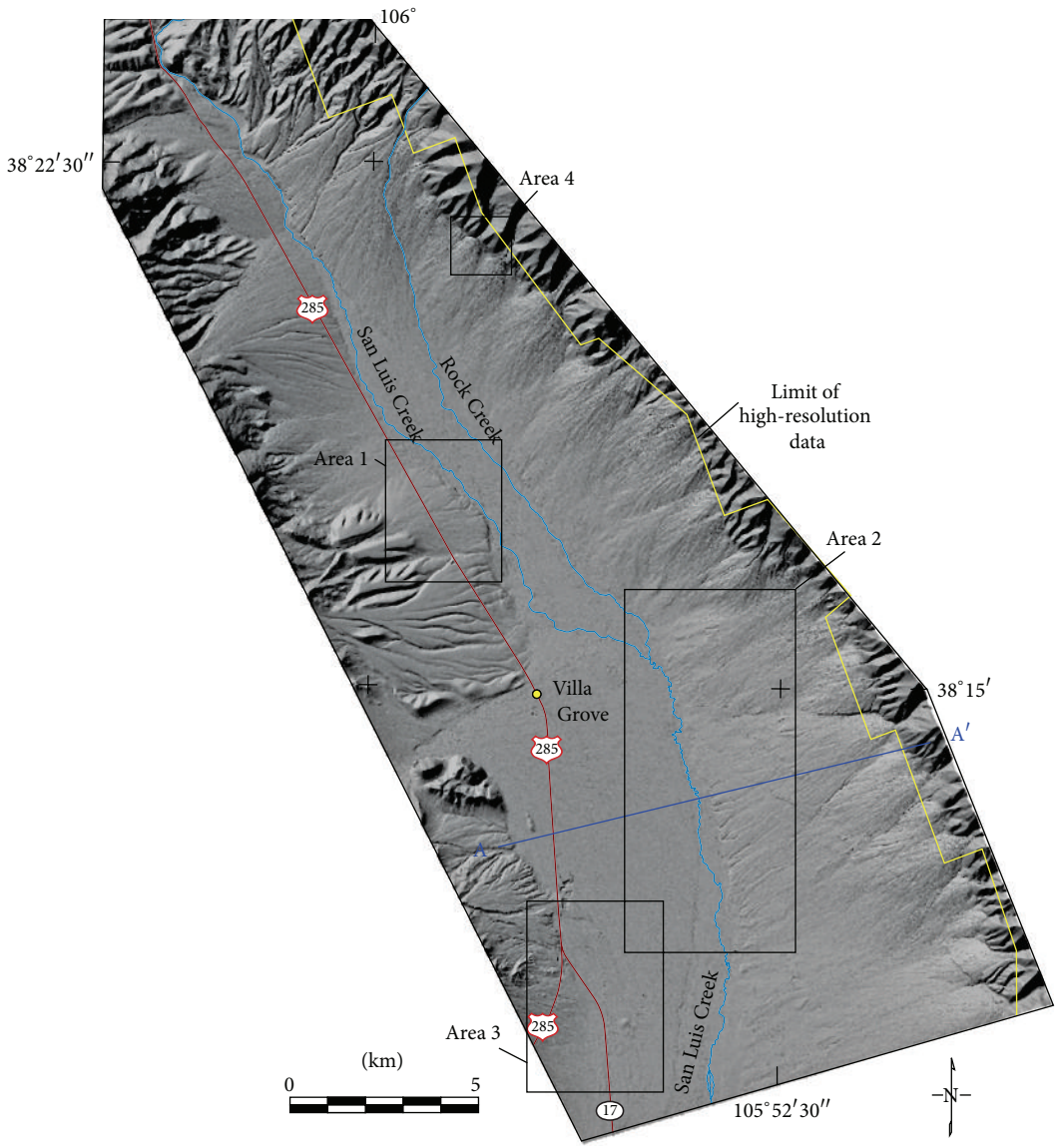

Figure 3: Northwest-illuminated hillshade of LiDAR data for the study area, graphically smoothed for viewing at page size. Yellow line indicates the limit of the high-resolution aeromagnetic data. Boxes locate example Areas 1–4. Model for A-A′ is shown in Figure 16.

sediments, the models can be applied to other layered geology as well, such as volcanic layers [47]. Moreover, as discussed by Grauch and Hudson [3, 47], the model layers represent magnetic contrast across the fault, rather than the geologic strata at the fault. The equivalent reduced-to-pole magnetic field and the magnitude of the horizontal gradient (the absolute value of the first derivative in the horizontal direction in the profile case) are computed for each model. The anomalies over two of the models (Figures 5(a) and 5(b)) are conventional fault-type anomalies and produce single HGM peaks for both the reduced-to-pole and magnetic potential computations. The anomaly shapes and multiple HGM peaks for the two other models (Figures 5(c) and 5(d)) are unconventional, but commonly observed. The models demonstrate that the narrowest HGM peak of the reduced-to-pole magnetic data most reliably locates the shallowest projection of the fault. Computing the HGM in two directions produces images where narrow ridges culminate over faults in map view. Although the horizontal gradient is commonly computed from the magnetic potential instead of reduced-to-pole data to avoid multiple HGM peaks over thin bodies [48, 49], this approach does not correctly locate the top projection of the fault for the two unconventional model cases (Figures 5(c) and 5(d)) [3].

Multiple parallel HGM ridges computed from reduced-to-pole aeromagnetic data are commonly observed on maps in the Rio Grande rift south of the study area [3]. Because parallel ridges can indicate multiple parallel normal faults

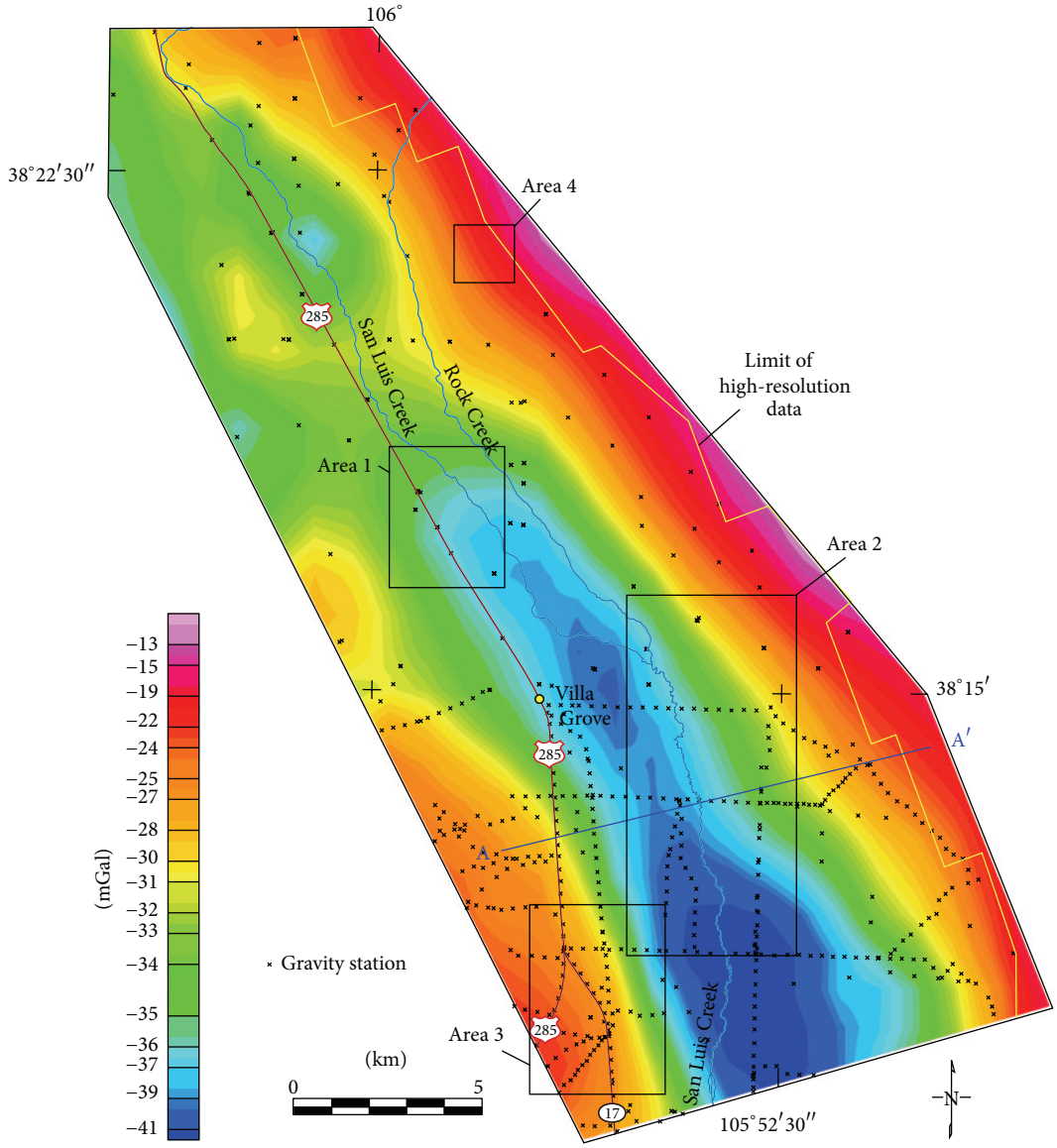

FIGURE 4: Isostatic residual gravity data showing station coverage. Boxes locate example Areas 1–4. Model for A-A′ is shown in Figure 16.

(e.g., Figures 5(a) and 5(b)) or a complicated geometry of juxtaposed layers that produce multiple ridges of variable amplitude (e.g., Figures 5(c) and 5(d)), Grauch and Hudson [3] developed some criteria to distinguish the cause. A complicated geometry is indicated by a pair of HGM ridges, where one ridge is narrower than the other. The narrower ridge (indicating a shallower source) best indicates the location of the fault where it reaches or nears the surface. Similar multiple parallel HGM ridges are observed in a computation of the HGM of the reduced-to-pole aeromagnetic data for our study area (Figure 6). Because of the presence of strong regional gradients that can swamp high-frequency signal from shallow faults, the HGM was computed using the gradient window method [50]. This method removes a best-fit regional trend within a window before computing the HGM across the grid. Afterwards, peaks in the HGM are located in the same positions as those that result from filtering the grid to focus on shallow sources before computing derivatives. However, it is much easier to test different window sizes to focus on removal of different regional gradients. We found a window size of 25 × 25 grid cells (1,225 m × 1,225 m) generally shows the best results for the study area, although other window sizes were also inspected (not shown).

Although HGM ridges were important criteria for identifying faults in the aeromagnetic data, other criteria were also used. Abrupt terminations or changes in aeromagnetic anomaly character or in the termination of HGM ridges along a linear edge also indicated faults. Conversely, not all linear HGM ridges represent faults. They may correspond to topographic scarps or other linear geologic features, such as contacts at the eroded edges of tilted blocks, dikes, or paleochannels.

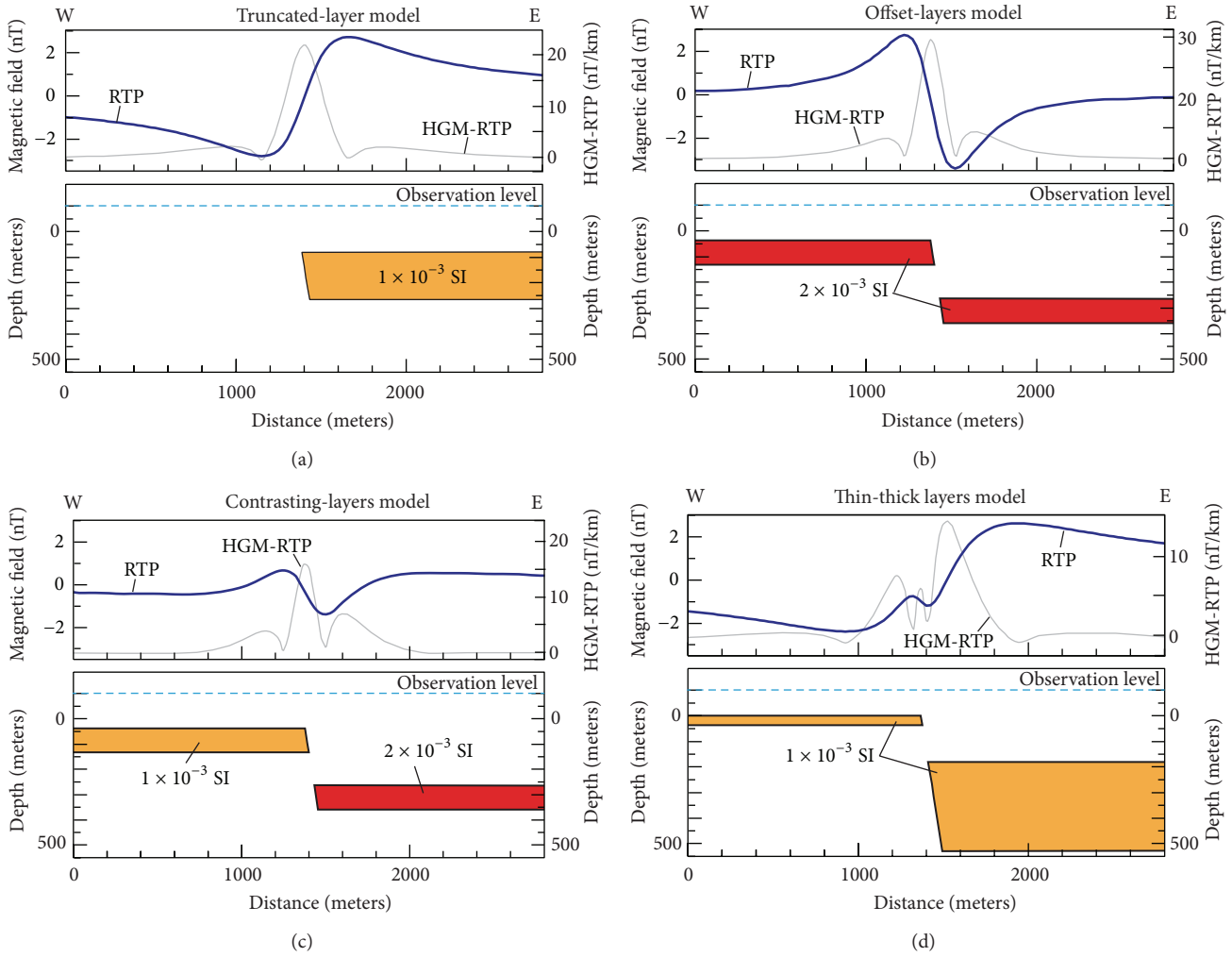

FIGURE 5: Simple 2D geophysical models illustrating the four main types of aeromagnetic signatures associated with intrasedimentary normal faults in the central Rio Grande rift. Model concepts can also be applied to other layered geology, such as volcanic flows. Profiles are computed for the reduced-to-pole magnetic anomaly (bold blue lines) and the horizontal gradient magnitude of the reduced-to-pole anomaly (HGM-RTP—solid gray lines). Magnetic susceptibilities are color coded and labeled.

4.2. Identifying Faults from LIDAR Data. Airborne LiDAR surveys provide extremely detailed digital maps of the elevation of the ground surface over large areas. The detail allows unprecedented views of the geomorphology, leading to the recognition of subtle, gently sloping fault scarps or other topographic expressions of faults that are time consuming to map using conventional methods. As demonstrated in the northern Rio Grande rift, mapping the geomorphology of surficial deposits also leads to identification of their relative ages, with younger deposits showing greater roughness than older ones [21, 31]. Thus, the general age of fault activity and sense of fault motion can be determined from the deposits that are displaced. In addition, digital slope profiles across fault scarps extracted from LiDAR data can be analyzed directly to estimate age of scarp formation [51]. On the other hand, mapping linear topographic scarps from surface evidence alone has limitations. First, fault scarps can be degraded or buried by surficial processes, hindering the mapping of their continuity along strike or their connection to other faults. Such discontinuity of fault scarps is common in the northern Rio Grande rift [24] because of the long intervals between earthquakes (10–140 ka) since early Pleistocene [4, 5, 52]. Second, some fault scarps may represent single-event splays of larger, more active faults that pose greater seismic hazards. Finally, fluvially trimmed stream-terrace deposits are sometimes difficult to distinguish from scarps of tectonic origin. Both produce steep topographic scarps and are easily degraded so that the origin is not evident. The ambiguity has caused debate over several linear topographic scarps within the northern Rio Grande rift [6, 53]. We examine this question in more detail for our study area in following sections.

Initial geologic mapping using LiDAR imagery identified the morphostratigraphic relationships between deposits of differing relative ages. The high-resolution imagery (<1 meter/pixel) permitted greater precision in differentiating surfaces with varying surficial morphologies. Older alluvial fan surfaces have less distinct microtopography (i.e., bar and

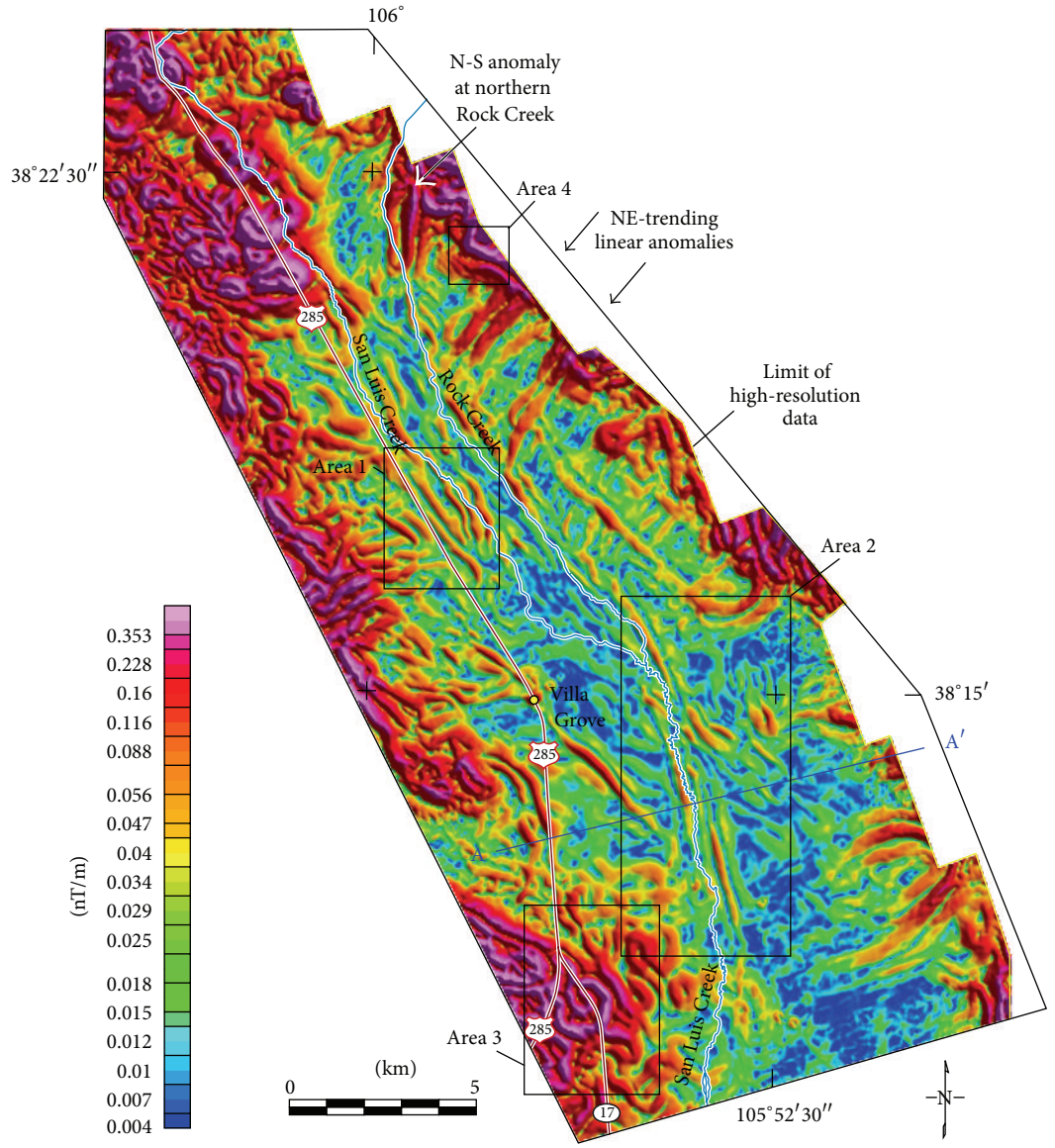

FIGURE 6: Horizontal gradient magnitude (HGM) of reduced-to-pole, high-resolution aeromagnetic data, using the gradient window method (window size = 1,225 × 1,225 m) to focus on gradients caused by shallow sources. HGM image is illuminated from the northeast. Boxes locate example Areas 1–4. Model for A-A′ is shown in Figure 16.

swale topography) and are generally more deeply dissected, indicating abandonment of the original deposition surface. Younger fan surfaces have very distinct bar and swale topography and generally grade to the active axial valley floodplain.

The relative position of these deposits and surfaces of differing ages is directly related to the geomorphic evolution of the region. Bull [54] demonstrated that, along tectonically active range fronts, younger alluvial fans are sequentially stacked at the mountain-piedmont junction. Along inactive range fronts, younger alluvial fans instead incise the fanhead and prograde farther out into the basin.

4.3. Combined Interpretation. Combined interpretation of aeromagnetic and LiDAR data builds on the strength of the aeromagnetic method to locate normal faults with significant offset under cover and the strength of LiDAR interpretation to identify the age and sense of motion of faults. Moreover, ambiguities in interpreting multiple HGM ridges from the aeromagnetic data can be resolved by examining which are associated with scarps in the LiDAR data. Uncertainty in resolving the tectonic versus fluvial origin of scarps next to streams identified by LiDAR data can be resolved by comparing the locations of HGM ridges in the aeromagnetic data.

Combined interpretation was done iteratively, by first identifying or interpreting faults in each dataset separately, then determining similarities and differences and resolving ambiguities by comparing results. The HGM ridges were commonly used to define the buried segments of faults in

between scarps identified in the LiDAR data. In some areas, faults inferred from the aeromagnetic data without associated scarps were considered to be potentially active if they were aligned with other active faults and/or followed gravity gradients defining gravity lows. The sense of motion for these inferred faults were assumed to be down into the basin as defined by the gravity low, although antithetic faults are possible.

5. Examples of Combined Interpretation

Examples of combined interpretation for four localities from our study area demonstrate different aspects of how aeromagnetic and LiDAR data were compared to resolve issues specific to the study area. Areas 1–4 are located on Figures 1–4 and 6.

5.1. Area 1 Example. Area 1 is located on the central west side of the valley in a low-relief area where basin-fill and alluvial deposits of several different ages are mapped (Figure 1). Reduced-to-pole aeromagnetic data for Area 1 indicate several narrow, northwest-trending linear anomalies superposed on a broader pattern of highs and lows (Figure 7(a)). The locations of the edges of these anomalies are more apparent as linear ridges in the HGM map (Figure 7(b)). These kinds of patterns are characteristic of shallow faults that displace sediments or rocks of differing magnetic properties, allowing faults to be interpreted along the peaks of the ridges, as described in Section 4.1. However, interpreting the multiple parallel HGM ridges in the central part of the area is uncertain. Recognition of pairs of ridges associated with one fault, where one ridge is narrower than the other (e.g., Figures 5(c) and 5(d)), is ambiguous because there are an odd number of ridges.

Deposits of five different ages for Area 1 are distinguished by variations in morphology of the land surface apparent in the LiDAR hillshade image (Figure 7(c)). They are mapped in Figure 7(d) as Holocene stream alluvium (Qh), Pleistocene glacial fan deposits (from the youngest to the oldest Qfy, Qfi, and Qfo), and Miocene-Pliocene rift fill (Ts). Several subdued, northerly linear breaks in slope cross the deposits (black lines across Qfo, Qfi, and Qh on Figure 7(d)). Scarps are most pronounced within the Holocene alluvium Qh; scarps across the older fans are more difficult to follow. The prominent topographic scarp adjacent to San Luis Creek is ambiguous from LiDAR data alone; it may be a fault scarp, the result of fluvial trimming, or both.

Comparing the HGM map to the LiDAR image provides greater confidence in locating faults (Figure 8). Scarps evident in the LiDAR image partially correspond to four of the multiple HGM ridges (faults A, B, C, and D on Figure 8), indicating these are the HGM ridges that best locate the traces of active faults. Moreover, the east-facing scarps in the LiDAR image suggest the faults are normal and down to east. The eastward offset of the aeromagnetic representation (white line) from the LiDAR scarp (black line) of fault A in the southeastern part of the area probably indicates variability in the source and depth of the magnetically contrasting layers along strike of fault A. In the very southeastern corner of the Area 1, the absence of aeromagnetic expression of fault A, but not its associated scarp, suggests that the fault does not terminate. Instead, the lack of aeromagnetic anomaly likely results from the juxtaposition of strata having similar magnetic properties, which produces no magnetic contrast.

The HGM ridges also help guide connections between scarps on the LiDAR image and suggest that these faults have significant displacement at depth. For example, the HGM ridge for fault A suggests that, from south to north, the fault extends toward a subtle scarp within the stream valley at the northern end of fault A as opposed to following the stream bank to the northwest along the contact between Qfi and Qh. The HGM ridge associated with fault C implies the fault underlying the slope expressed in the LiDAR south of the contact of Qfi and Qfo extends towards the northwest, rather than to the north, where it is tempting to make a connection to the slope associated with fault B (compare Figure 7(d)). The strong northwest-trending HGM ridge near D appears related to the northwest-striking portion of the scarp just south of D and suggests that this fault continues to the northwest underneath Qfi. Fault E is identified aeromagnetically by a break in pattern of HGM ridges that indicate a sharp difference in lithology along a linear contact. Its fault origin is supported by the two nearby scarps determined from the LiDAR data (more evident in hillshade images of different illuminations than shown in Figure 7(c)).

The LiDAR data are important for determining relative age of faults interpreted for Area 1. Fault A has been active most recently, because a scarp is developed in Holocene deposits (Qh). The most recent event for fault B occurred <170 ka but >10 ka (post-Qfi and pre-Qh), because a scarp is apparent in Qfi but not in Qh. The most recent event for fault C occurred <640 ka and >120 ka (post-Qfo and pre-Qfi) and for fault E occurred since 120 ka (post-Qfi). The most recent activity on Fault D, which connects two scarps that displace Qfi, likely occurred <170 ka.

A magnetic model was constructed along a southwest to northeast profile across Area 1 (Figure 9). The model is highly uncertain because of poor constraints on subsurface geology, variable thickness and/or magnetic properties of geologic units in the area, and paucity of gravity data for Area 1 (Figure 4). Moreover, this type of geologic variability tends to produce multiple magnetic sources that are inconsistently related to geologic contacts at depth, making it difficult to interpret the results of standard quantitative techniques, such as depth estimation [3]. Nevertheless, the model helps visualize the multiple sources that are potentially contributing to the observed aeromagnetic anomalies at faults.

Model units were assembled on the basis of geologic concepts, inspection of aeromagnetic maps, and reconnaissance magnetic-susceptibility measurements of outcrops within and near the study area. Magnetic susceptibilities of Holocene stream deposits (Qh) are generally 0.0005 SI or lower, whereas those measured for Quaternary fan material (Qfy, Qfi, and Qfo) range from 0.0010 to 0.0100 SI, with a mode of ~0.0060. The latter values are fairly magnetic for sediments but are within the ranges observed for sediments in the northern Rio Grande rift [46, 47]. We estimate that the collective thickness of the Quaternary deposits generally

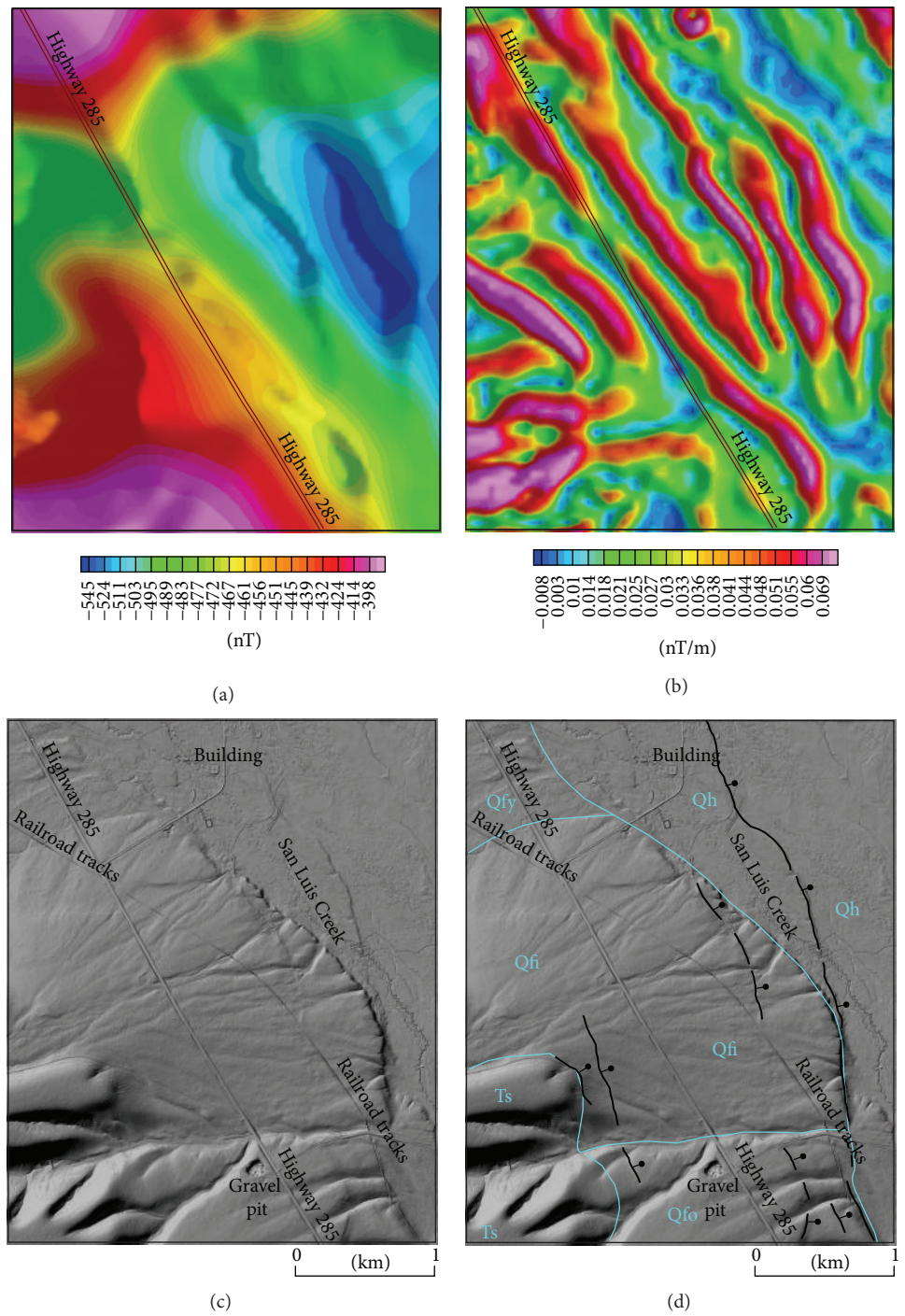

Figure 7: Aeromagnetic and LiDAR data for Area 1 (located on Figures 1–4 and 6). (a) Reduced-to-pole (RTP) aeromagnetic data and (b) horizontal-gradient magnitude (HGM) of RTP. NW-illuminated hillshade of LiDAR data, without (c) and with (d) inferred faults and contacts (cyan lines) overlain. Geologic units are explained in Figure 1.

ranges from 10 to ~100 m. Thicknesses, lithologies, and magnetic properties of the underlying Tertiary rift sediments (Santa Fe Group) are highly uncertain. However, similar to observations in the central Rio Grande rift [46], we expect that the sediments are stratified in layers of differing magnetic susceptibilities, with average values ranging from ~0.0005 to 0.0030 SI. How such layers are arranged in the subsurface of our study area is unknown, but the history of tectonic activity [19, 31] suggests that coarse-grained sediments, representing the more magnetic of the sediments, likely lie toward the base of the section and thicken into the deepest parts of the basin. Reconnaissance magnetic-sus-

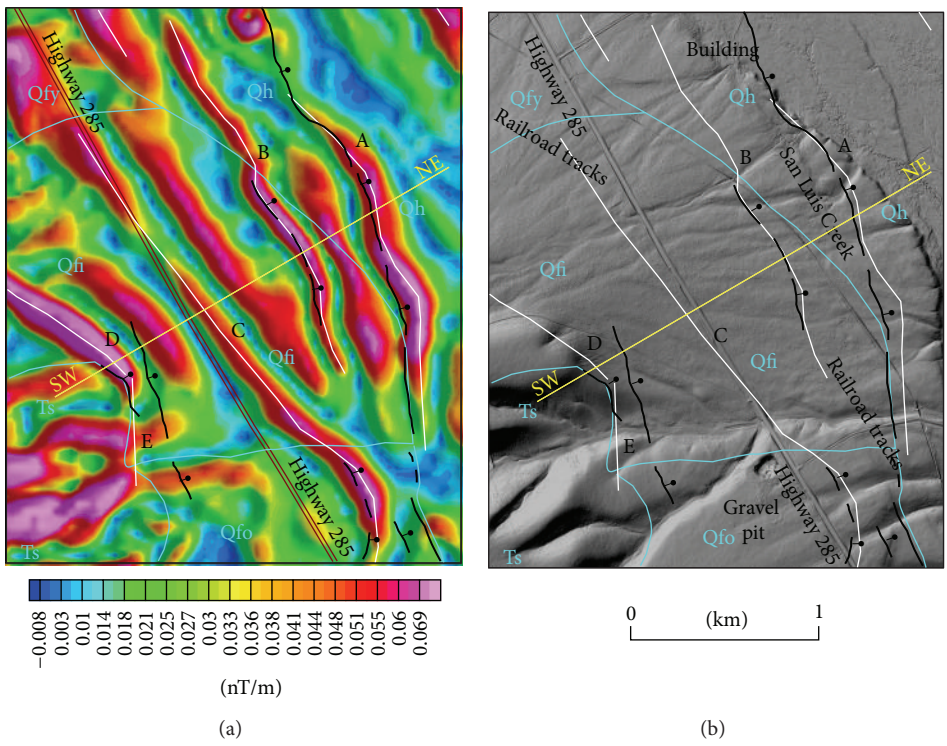

Figure 8: Combined interpretation for Area 1 (located on Figures 1–4 and 6). Faults mapped from LiDAR are in black; those interpreted from ridges in HGM image (Figure 6) are in white. Geologic contacts mapped from the LiDAR data are in cyan. Geologic units are explained in Figure 1. Letter labels refer to faults discussed in text. (a) HGM map of the reduced-to-pole aeromagnetic data; (b) NW-illuminated hillshade of LiDAR data. Model for southwest to northeast profile (SW, NE) is shown in Figure 9.

ceptibility measurements of Precambrian rocks in our study area range from <0.0010 to ~0.0250 SI, similar to the range of values found immediately to the north of our area [40, 55]. High-amplitude aeromagnetic anomalies over exposed Proterozoic rocks to the west of the study area suggest that these rocks are fairly magnetic underneath Area 1, so we assign a value of 0.0100 SI.

The model of Figure 9 demonstrates that the juxtapositions of lithologies of differing magnetic properties are the likely sources causing the observed (reduced-to-pole) signal at faults A, B, C, and D for Area 1 (Figure 8). Moreover, multiple HGM peaks in between these inferred faults likely arise from magnetic contrasts at different levels of the faults rather than separate faults. An exception is the HGM peak just to the west of C that does not offset Qfi deposits (Figure 8) and occurs at about 1.5 km distance on the profile (Figure 9). A concealed, major rift fault is modeled at this location, which is required if prerift rocks have the same magnetic properties throughout Area 1. If this interpretation is correct, the concealed fault accommodates much of the vertical displacement at the western basin margin. An alternative model would involve a large magnetic discontinuity within the prerift rocks instead of a rift fault.

To illustrate the relative contributions of different magnetic sources to the overall computed field of the model, the computed field for each of three different groupings of model bodies is also shown on Figure 9. These three curves add together to form the computed field for the whole model. As expected, the computed field of the prerift model units accounts for the broad character of the observed field, with significant contribution to anomalies over faults where the prerift rocks are shallower. The modeled Quaternary units (Qh and Qf) account for most of the character of the short-wavelength anomalies over the faults. The computed field from the Tertiary rift-fill sediments (Ts1 and Ts2) has the least contribution to the character of the whole computed field, so the choice of layers within this model unit does not have significant impact on the model results.

5.2. Area 2 Example. Area 2 is located in the valley and on fan material on the southeastern part of the study area where the swarm of northwesterly normal faults known as the Villa Grove fault zone has been mapped (Figure 1). These faults are quite evident as curvilinear scarps in an enlarged area of the LiDAR image (Figures 10(a) and 10(b)), located on the inset of Figure 10. In contrast to Area 1, there are many more scarps than identifiable HGM ridges in this area (Figure 10(c)). The HGM ridges, except in the northern and western parts of the enlarged area, are also more subdued. Similar to examples shown for Area 1, the differences in HGM amplitudes may be a function of variations in the deposits that are juxtaposed at depth along strike of the faults.

Many of the scarps evident in the LiDAR image are likely secondary features of mass wasting related to more major faults and located in between them [8, 10, 21]. The major faults can be identified by the HGM ridges because the ridges

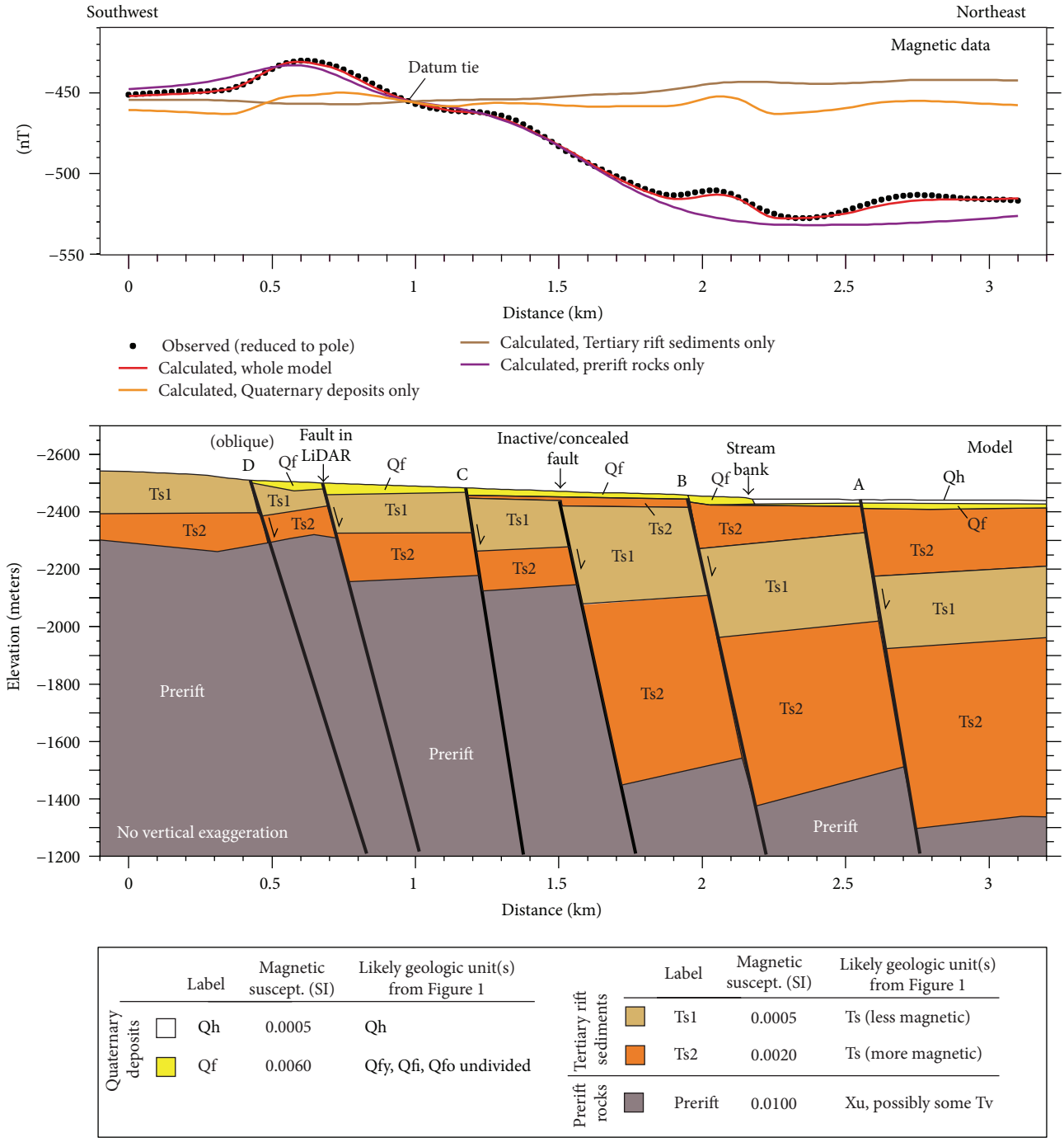

FIGURE 9: 2D magnetic model for the southwest to northeast profile across Area 1 (located on Figure 8). Observed curve was extracted from the reduced-to-pole aeromagnetic grid (Figure 2). Reasoning behind the magnetic model parameters and uncertainties in the model results are discussed in the text. Letter labels along the ground surface refer to the letter labels in Figure 8.

indicate significant offset between materials of differing magnetic properties. For example, a major fault is represented by the prominent scarps in the LiDAR image that follow HGM ridges from A to B to C (Figure 10). Both the LiDAR and HGM images suggest the fault anastomoses at B. Other major faults can be traced by HGM ridges that coincide with scarps that pass northeast of A and southwest of D. All these scarps are southwest facing in the NE-illuminated LiDAR image (scarps are in shadow) and, thus, down to the southwest. The offset to the southwest of the HGM ridge related to the scarp at E is likely the result of magnetic contrast that is downdip from the surface trace. The scarps southwest of the two locations of F are northeast facing (scarps are highlighted) and probably represent antithetic faults down to the

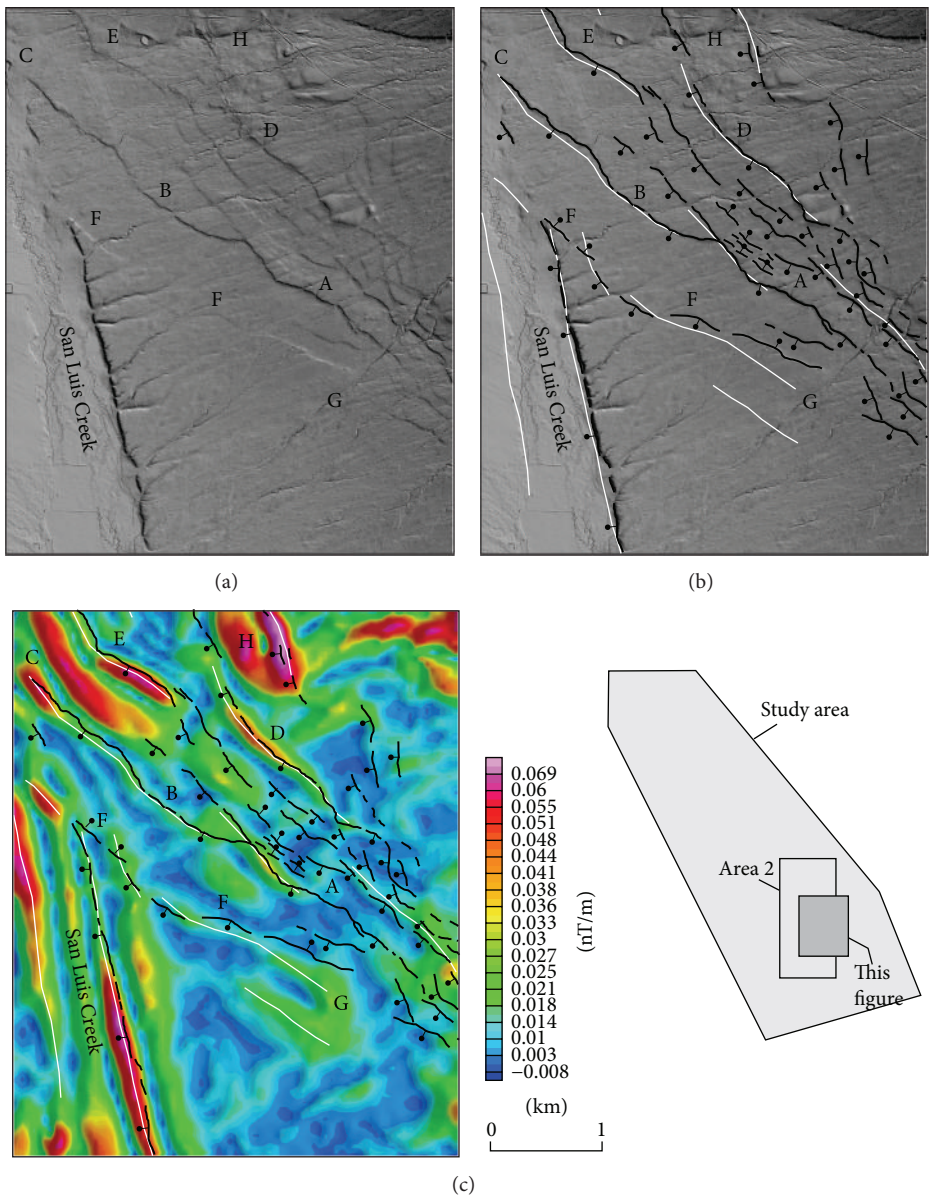

Figure 10: Example of combined interpretation for enlarged area related to Area 2 (inset). Faults from the LiDAR interpretation are black and those mapped from HGM image (Figure 6) are white. Letter labels are for discussion purposes. NE-illuminated hillshade of the LiDAR data without (a) and with (b) faults overlain. (c) HGM of reduced-to-pole aeromagnetic data with faults overlain.

northeast. The HGM ridge at G that parallels the northeast-facing scarp to the southwest is not likely associated with the deeper parts of fault F. If it were, it would be offset to the northeast instead. Several northeast-facing scarps northwest of A likely represent secondary antithetic faults as well.

Most of the scarps of the Villa Grove fault zone are well defined as they cross both younger (Qfy) and intermediate-age fan material (Qfi) (Figure 1), indicating the most recent fault activity was fairly young (<15 ka). By contrast, scarps east and west of H, which cross Qfo, are more degraded and discontinuous (Figure 10(a)), implying that these faults may not have ruptured during the most recent event.

The prominent stream bank on the eastern side of San Luis Creek (Figures 10(a) and 10(b)) could be interpreted geomorphologically as a fault scarp or a fluvially trimmed terrace deposit. Ruleman and Machette [10] suggest a tectonic rather than fluvial origin because of the linearity of the topographic scarp and the absence of a paired terrace deposit on the west side of the creek. However, similar geomorphic features south of our study area are still under debate by geologists [53]. The presence of linear HGM ridges coincident with the linear topographic scarp provides support for a tectonic origin. The narrowness of the HGM ridges advocates near-surface, near-vertical boundaries for the magnetic sources [56]; their linearity supports a fault contact rather than a facies change. Near-vertical, distinct magnetic contrasts, required to produce an HGM ridge, are difficult to explain by facies changes caused by depositional

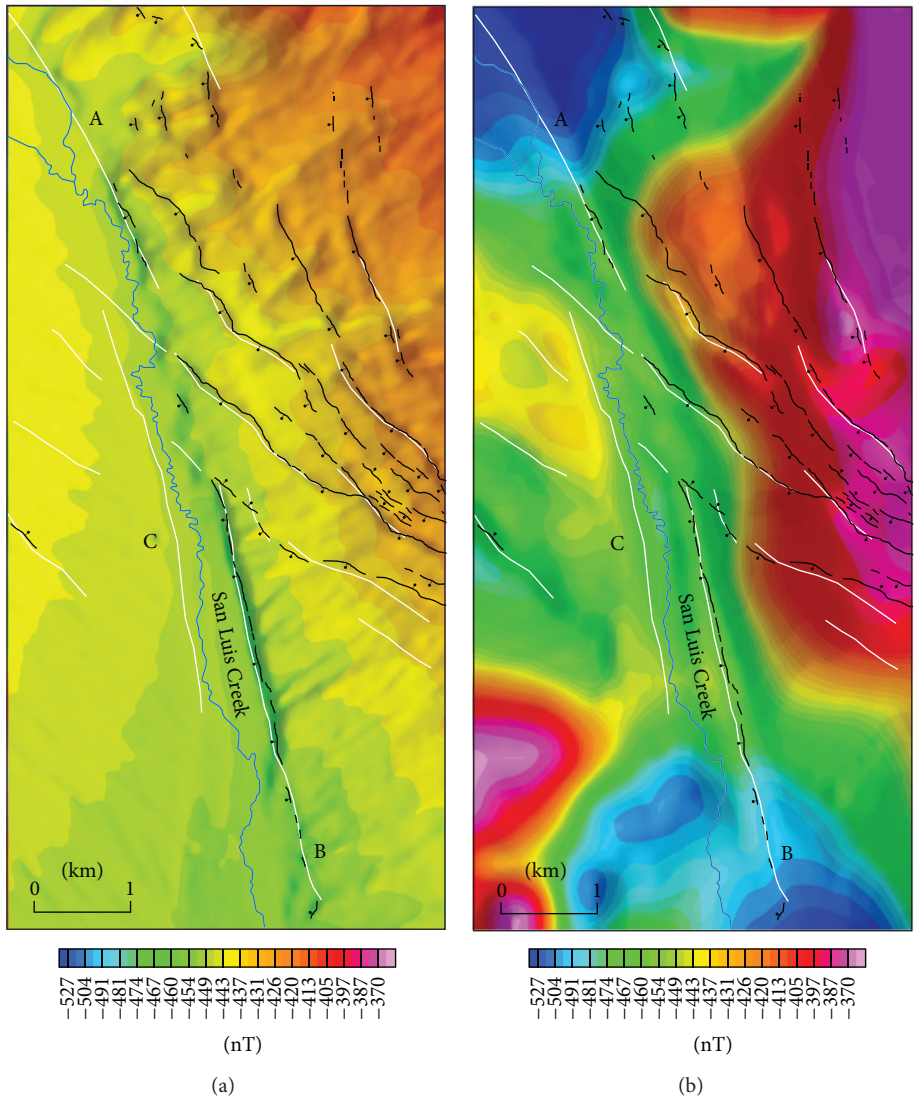

Figure 11: Assessment of terrain effects for Area 2. Hypothetical terrain effects in (a) are compared to patterns in the observed RTP aeromagnetic data in (b) to identify anomalies caused solely by topographic relief formed on magnetic Quaternary deposits. Note the lack of correlation along the stream bank on the east side of San Luis Creek. Faults from LiDAR (black) and those from HGM of RTP data (white) are overlain. Letter labels are for discussion purposes. (a) Hypothetical magnetic field computed from digital elevations using uniform magnetic susceptibility of 0.010 SI and height and Earth's field parameters to match the RTP observed data. Digital elevations for the computation were derived from the LiDAR data, gridded at 25-m interval. (b) Observed RTP aeromagnetic data. Northeast illumination and color scales are identical for both images.

processes. Because streams migrate laterally through time as the basin subsides, facies changes in the sedimentary section are likely to develop interfingered, irregular contacts when viewed in cross-section rather than sharp boundaries that extend to a significant depth.

However, linear topographic scarps can produce aeromagnetic anomalies even if they are not fault scarps [3]. To test whether the HGM ridges at the eastern bank of the San Luis Creek are caused by magnetic terrain effects or by underlying sources, we compute a model of hypothetical terrain effects for Area 2 (Figure 11(a)). The hypothetical model uses a digital elevation model and a uniform magnetic susceptibility of 0.010 SI to simulate anomalies due solely to the irregular topographic forms of surficial Quaternary deposits. The computation is accomplished by adding the effects of vertical prisms at each grid interval of the digital elevation model whose top is the average elevation of the surrounding grid points (J. Phillips, unpublished computer program MBOXES).

If all the underlying material in Area 2 were uniformly magnetized with magnetic susceptibility of 0.010 SI, the morphology of the top surface of the surficial deposits alone should produce aeromagnetic anomalies with amplitudes detectable by the aeromagnetic survey, as demonstrated by Figure 11(a). However, comparison to the observed reduced-to-pole aeromagnetic map (Figure 11(b)) shows that (1) an

aeromagnetic low is observed over the crest of the stream bank instead (Figure 11(b)), so the stream bank is not a significant source of the observed anomalies, and (2) observed aeromagnetic anomalies generally have greater amplitude than reasonably produced by relief on the terrain alone. Furthermore, HGM ridges follow straighter lines than the stream bank scarps and are continuous across places where the bank has been eroded, such as at A and B on Figure 11. A very linear HGM ridge follows the western stream bank beside C. The magnetic field produced by this stream bank is too subdued to produce the observed aeromagnetic gradient; an additional magnetic source is required at depth. Its similarity in linearity and parallel orientation to the HGM ridge over the eastern stream bank suggests that both HGM ridges are produced by faults in the subsurface.

Thus, we conclude that the HGM ridges along the stream bank originate from magnetic sources that underlie the terrain and the linearity of the ridges suggests a tectonic rather than fluvial origin. The HGM image for the whole study area (Figure 6) suggests that similar faults closely follow San Luis Creek and Rock Creek almost the entire axis of the valley within the study area.

The HGM image for Area 2 can be used to better understand the intersection of the Villa Grove fault zone and the San Luis Creek and Rock Creek fault zones (Figure 12). HGM ridges of the northwest-striking faults of the Villa Grove fault zone clearly cross and interrupt the more northerly HGM ridges related to the San Luis Creek fault (B, C in Figure 12) and the Rock Creek fault zone (A). The Villa Grove fault zone extends west of the San Luis Creek fault zone to D, where it is concealed beneath Holocene material. If the HGM ridge at C is a deeper manifestation of the magnetic contrast expressed at the HGM ridge at A, one could argue that the San Luis Creek fault is displaced down to the southwest relative to the Rock Creek fault at A. The Rock Creek fault zone gradually bends more westerly north of A (Figures 6 and 12), which may also be influenced by the younger Villa Grove fault zone.

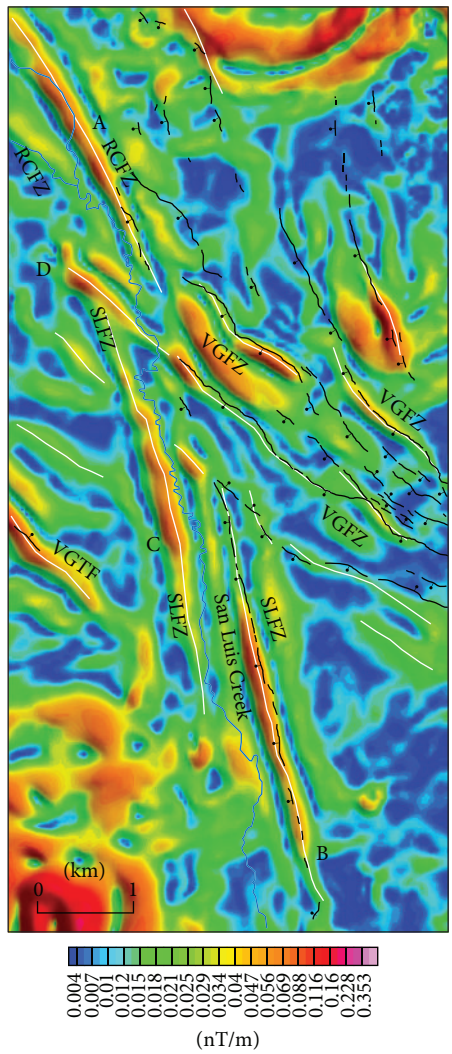

Figure 12: Ridges in the HGM of RTP image depicting the crossing of the Villa Grove and San Luis Creek fault zones in Area 2 (located in Figures 1–4 and 6). Letter labels are for discussion purposes. RCFZ: Rock Creek fault zone, SLFZ: San Luis Creek fault zone, VGFZ: Villa Grove fault zone, and VGTF: Villa Grove town fault.

5.3. Area 3 Example. Area 3 is located in the southwestern part of the study area near the western margin of the rift valley (Figure 1). Although the area has low relief, exposures of Proterozoic rocks (Xu) and high-amplitude aeromagnetic anomalies indicate that bedrock is close to the surface over most of the western part of the area (Figure 13). A north-northwest trending normal fault has been previously mapped at the basin margin (red on Figure 13). It passes near the Joyful Journey Hot Springs (previously known as Mineral Hot Springs) and related travertine mounds and is presumed to have an influence on the location of the upwelling thermal waters. The mapped Mineral Hot Springs fault is commonly extended farther south (out of the study area) to connect to the eastern bounding fault of a large intrarift horst concealed within the San Luis basin (e.g., [23]). Several workers argue that a scarp developed in Quaternary deposits (units Qfi and Qfy) along the Mineral Hot Springs fault indicates it is active; others contend that the scarp is an erosional feature (described in Kirkham [6]). Thus, combined interpretation of aeromagnetic and LiDAR data in this area can address this debate and serves as an example of interpreting basin-bounding as well as intrabasin faults from the aeromagnetic data.

Scarps mapped for the Mineral Hot Springs fault are indicated at locations marked A on the LiDAR image (Figure 13(a)), where a linear gradient is superposed on a broader aeromagnetic high (Figure 13(b)). On the north, the aeromagnetic low between locations marked as C (Figure 13(b)) generally corresponds to the westward extension of a normal fault that juxtaposes Proterozoic rocks (Xu) against effectively nonmagnetic Paleozoic sedimentary rocks (Pz). The fault is exposed just west of the northwest corner of Area 3 (Figure 1).

The extension of the mapped Mineral Hot Springs fault inferred southeast of B (dashed red line) is not supported by the aeromagnetic data. Instead, dominant features of the aeromagnetic data are (1) a north-northeast-trending, steep

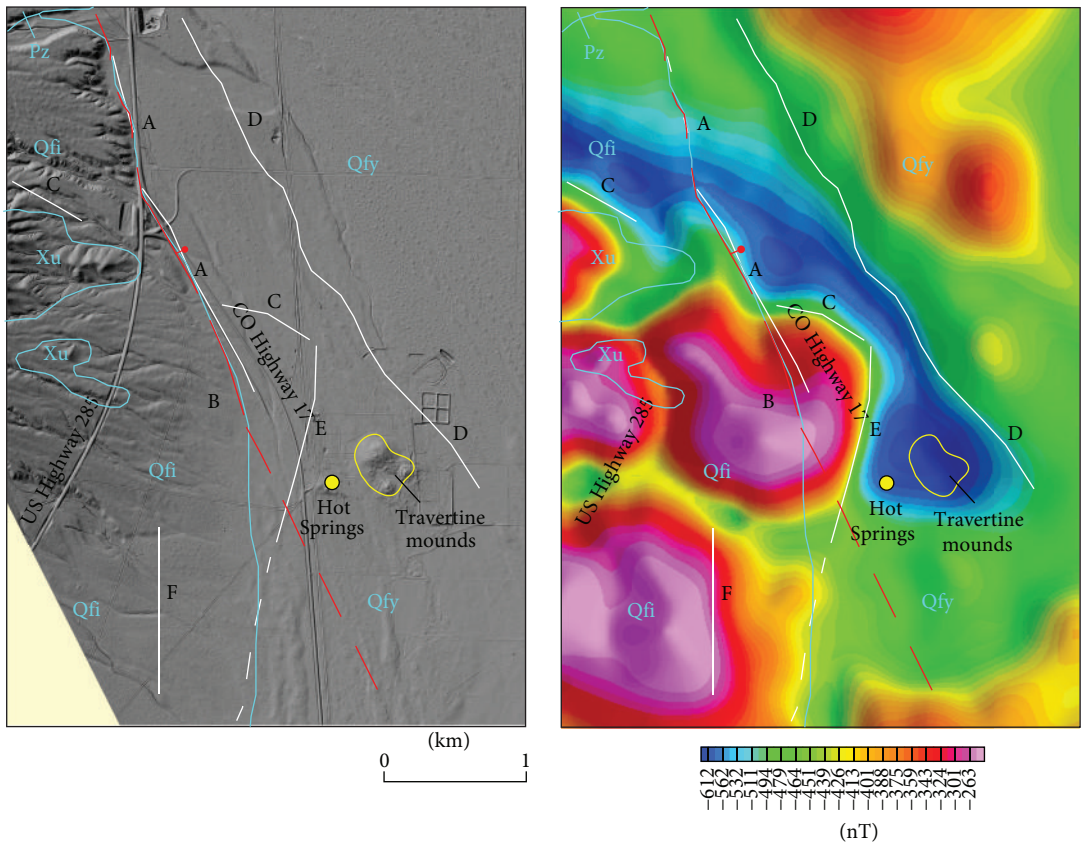

Figure 13: Example of combined interpretation from Area 3 (located in Figures 1–4 and 6) suggesting a revision to the location of faults surrounding the active hot springs. Previously mapped Mineral Hot Springs fault [6] is shown as solid and dashed red line. Lines interpreted from the HGM image (Figure 6) are in white. Geologic contacts (cyan lines) and units are from Figure 1. Letter labels are for discussion purposes. (a) NW-illuminated LiDAR image. (b) Reduced-to-pole aeromagnetic data, illuminated from the east.

gradient at E between strong highs on the west and subdued low values on the east that passes west of the hot springs; (2) a northwest-trending linear gradient between low values on the west and moderately high values on the east that passes east of the hot springs (locations D on Figure 13(b)); and (3) a north-south gradient at F. Both features D and E are interpreted as faults, although neither is associated with scarps in the LiDAR data. They surround a triangular shaped aeromagnetic low centered over the hot springs and related travertine mounds, suggesting a geologic association with the active geothermal system. The eastern one (D) is likely rift related, because of its orientation and location at the rift margin that follows trends in the gravity data (Figure 4). If so, fault D has not been active since >12 ka, when unit Qfy was deposited. We interpret the western faults at E and F as inactive, because their strikes do not align with the rift. The aeromagnetic low just east of E may indicate that Proterozoic rocks are juxtaposed against Paleozoic rocks at the inactive fault. The low also could be associated with secondary alteration of crystalline rocks that has destroyed the magnetic minerals. Perhaps thermal waters are currently rising within a fault-bounded hydrogeologic window in the area of the hot springs.

5.4. Area 4 Example. Area 4 is located at the high mountain range front, where the northwest-striking Sangre de Cristo fault follows the base of precipitous facets in the northeastern part of the study area (Figure 1). The LiDAR image clearly shows the fault as thin bands of shadow and highlight near the interface between the steep bedrock slopes and dissected alluvial fans (Figure 14(a)). The high resolution in the LiDAR display of the morphology of the fan surfaces allows detailed mapping of the fault and Quaternary deposits of three different ages (Figure 14(b)). Recurrent displacement along the fault zone is documented east and southeast of A by a sliver of intermediate-age fan material (Qfi) that is stranded and perched on the footwall. This fan was faulted after deposition, younger fan material (Qfy) progressively accumulated across the fault and covered the older fan on the downthrown side, and then both were ruptured during a later event. In the same vicinity (southwest of A), the Sangre de Cristo fault is evident crossing an area mapped as Proterozoic unit Xu. Faulting here has displaced the bedrock and/or colluvium within the footwall, implying that the fault has encroached into the footwall over time rather than stepped farther basinward, as is commonly expected in extensional basins.

In contrast to the detail of the LiDAR image, the aeromagnetic data for Area 4 are dominated by high values on the northeast, which increases almost 300 nanoTeslas over a distance of only about 1.5 km along a northwest-trending gradient (Figure 14(c)). A large component of the high is likely caused by magnetic Proterozoic rocks within the steep terrain, as evidenced by a general correspondence of the bedrock terrain to anomaly shape at locations marked B. However, the northwest-trending gradient does not exactly follow the base of the mountain front (compare the locations of the scarps to the HGM ridges on Figure 14(d)), which would be expected if the gradient were reflecting solely terrain shapes. Differences in Proterozoic rock type likely also contribute to the aeromagnetic expression, as evidenced by a prominent north-northeast trending ridge in the HGM image (C on Figure 14(d)) that does not correspond to slopes in the terrain. Thus, we suspect that the Sangre de Cristo fault zone is partially following older structures, probably related to Laramide thrust faulting or early rift faulting in the Miocene. If so, the structure is somewhat oblique to the extension direction. A relation between Laramide thrust faults and the Sangre de Cristo fault has been noted for this area previously [57]. Linear breaks in slope superposed on the larger regional gradient in the aeromagnetic data are mostly evident in the HGM image (D on Figure 14(d)). They are interpreted as potentially active rift-related faults because they parallel the range-front fault.

Identifying and characterizing active faults are straightforward from the LiDAR data at the range front, where active fan deposition and faulting are clearly expressed in the geomorphology. Isolating the expression of Quaternary faults in the aeromagnetic data is more difficult, because highly magnetic sources in the Proterozoic bedrock dominate the aeromagnetic signal and are the product of multiple events over geologic history. However, using both LiDAR and aeromagnetic data together could provide insights into older, underlying structures and their possible influence on the propagation of seismic energy during an earthquake.

6. Results

Generalized faults identified by combined interpretation of the aeromagnetic and LiDAR data are presented in Figure 15. Faults were classified by the age of their most recent rupture and relations to other active faults. Younger active faults show LiDAR evidence of displacement of the younger Quaternary units, so they ruptured <10 ka (post-Qh) or <30 ka (post-Qfy). Older active faults displace the older units, so they ruptured between 120 ka and 170 ka (post-Qfi) or between 170 ka and 640 ka (post-Qfo) or are cross-cut by younger active faults. Faults identified by the aeromagnetic data only are considered potentially active if (1) they are buried by any of the Quaternary deposits; (2) they align with trends of active faults nearby, or (3) a combination of these. If faults identified solely by aeromagnetic data do not meet the criteria of a potentially active fault, they are considered inactive and concealed (Figure 1). The sense of displacement of normal faults was determined primarily from the orientation of scarp faces apparent from the LiDAR data. They were inferred from gravity data where scarps were not present and the inferred faults followed gravity gradients, although local structures violating this assumption are possible. Modifications to the mapping of Quaternary deposits were recognized while determining the age of faulting. These modifications are depicted generally on Figure 15 as well.

Both the LiDAR and aeromagnetic data (where they cover the range front) suggest the Sangre de Cristo fault is segmented along the northwest strike of the range front and can have multiple discontinuous strands parallel to each other, some of which may be represented by potentially active faults. The Villa Grove fault zone is similar in character as mapped previously, but the aeromagnetic data indicate which of the multiple faults may have experienced the most displacement. The Villa Grove town fault, named herein, suggests that poorly defined faults mapped previously extend for 5–7 km and pass through the town of Villa Grove. The Mineral Hot Springs fault is revised to apply to an inferred fault in the aeromagnetic data underneath Holocene deposits that parallels the previously inferred fault at the stream bank but passes on the east rather than west side of the hot springs. Faults are evident along both San Luis Creek and Rock Creek, supporting a tectonic or fluvially modified tectonic origin for steep scarps located at stream banks. The aeromagnetic data provide additional information about their extents in between discontinuous scarps and suggest several totally buried, potentially active faults are present on both sides of the valley.

7. Discussion

7.1. Two-Dimensional Model. The nature of the rift in relation to the active faults in the valley is further elucidated by a two-dimensional (2D) geophysical model along a roughly east-west profile A-A′ (Figure 16), located on Figures 2–4, 6, and 15. Modeled geologic units were assigned magnetic susceptibilities as described in Section 5.1 regarding the 2D model for Area 1 (Figure 9), except that Holocene unit Qh was grouped with the older Quaternary units because of the more regional scale of this model. Densities were assigned within the ranges of values we measured from similar geologic units in the region and from published sources [40, 43, 55]. As discussed in Section 5.1, thicknesses and/or magnetic susceptibilities of the Tertiary and Precambrian basement rocks are poorly constrained. Thus, we have kept the model as simple as possible. A more complex model could fit the data better but adds greater uncertainty.

The 2D model for A-A′ supports evidence from the gravity map (Figure 4) that the axis of the rift lies between San Luis Creek and the Villa Grove Town fault, with the Villa Grove fault zone and the Mineral Hot Springs fault as the eastern and western margins, respectively. Unlike the east-dipping half graben with large-displacement master fault at the range front that is commonly described for the main San Luis Basin to the south, this basin is located well to the west of the range front. Instead, vertical displacement at the range-front fault is on the order of 100 m. The bedrock surface dips at fairly low angle westward from the range front to the Villa Grove fault zone, which forms a broad zone along the east-

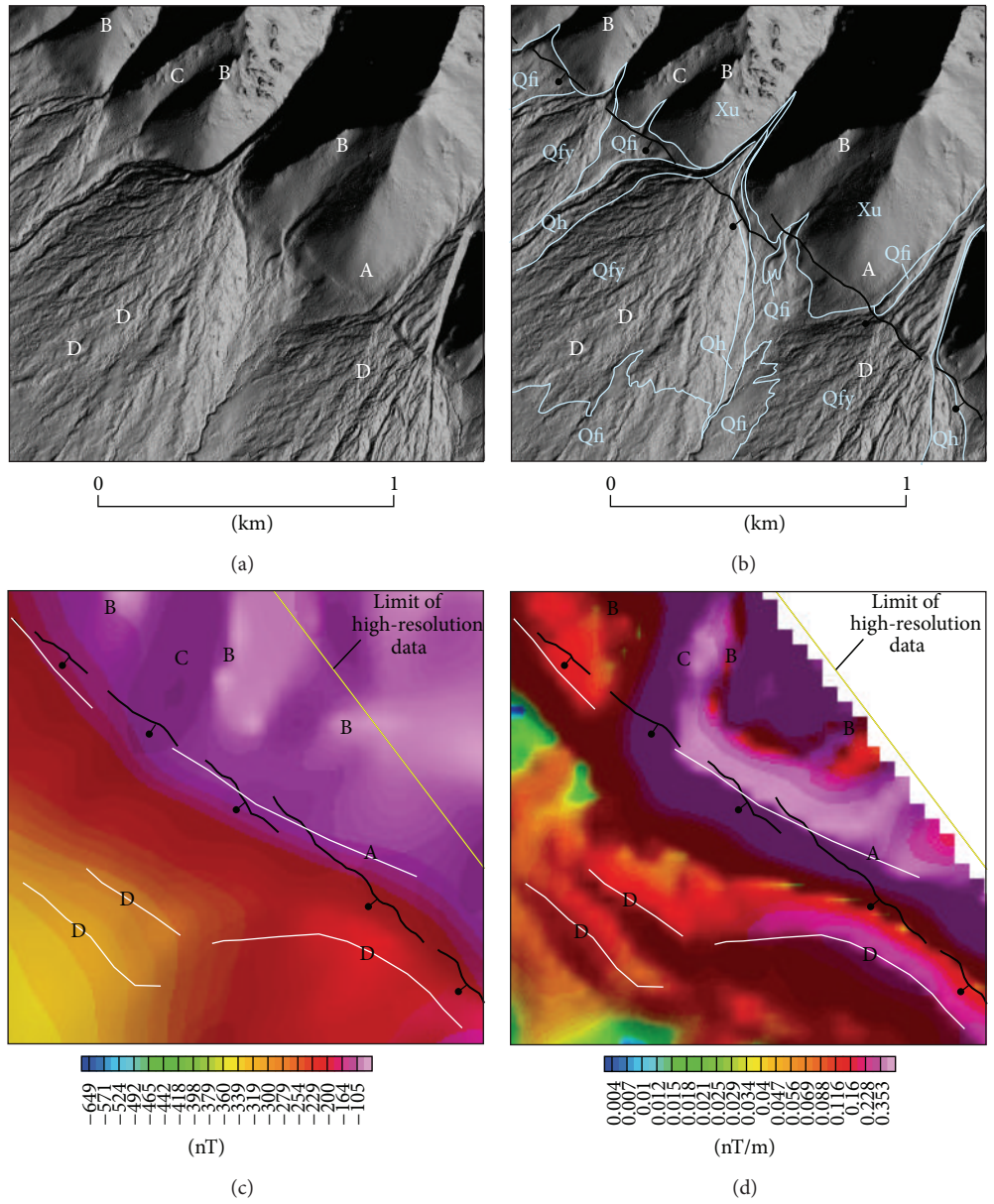

Figure 14: Example of combined interpretation from Area 4 (located in Figures 1–4 and 6). Black lines are scarps mapped from the LiDAR image; white lines are faults inferred from the HGM image. Letter labels are for discussion purposes. (a) LiDAR hillshade image, illuminated from the southeast. (b) The same LiDAR image with detailed mapping of Sangre de Cristo fault (black line) and Quaternary deposits (cyan lines). Geologic codes are as in Figure 1. (c) Reduced-to-pole aeromagnetic image illuminated from the east. (d) HGM of reduced-to-pole aeromagnetic data, illuminated from the northeast.

ern margin of the rift basin. Hypotheses to explain the low-angle slope are (1) a relic of previous tectonic activity, such as Laramide thrust faulting; (2) the result of early-rift detachment faulting; or (3) the product of regional tectonic tilting to the west related to early rifting. In any case, the focus of tectonic activity apparently has been concentrated in the vicinity of San Luis Creek, where most of the displacement and basin subsidence has occurred. Tectonic activity at the range front must have started late in rift history, as evidenced by the relatively small displacement across the fault there.

The curve extracted from the HGM grid in the top panel of Figure 16 emphasizes the utility of computing the HGM using the gradient window method to detect the subtle signature of faults in the aeromagnetic data. The HGM curve peaks over subtle gradients caused by shallow sources within the surficial deposits where the smaller gradients can be masked by broad regional magnetic gradients. Individual faults (except the Mineral Hot Springs fault) have even less expression in the gravity profile. The lack of expression is especially noticeable along the broad, almost linear, decrease

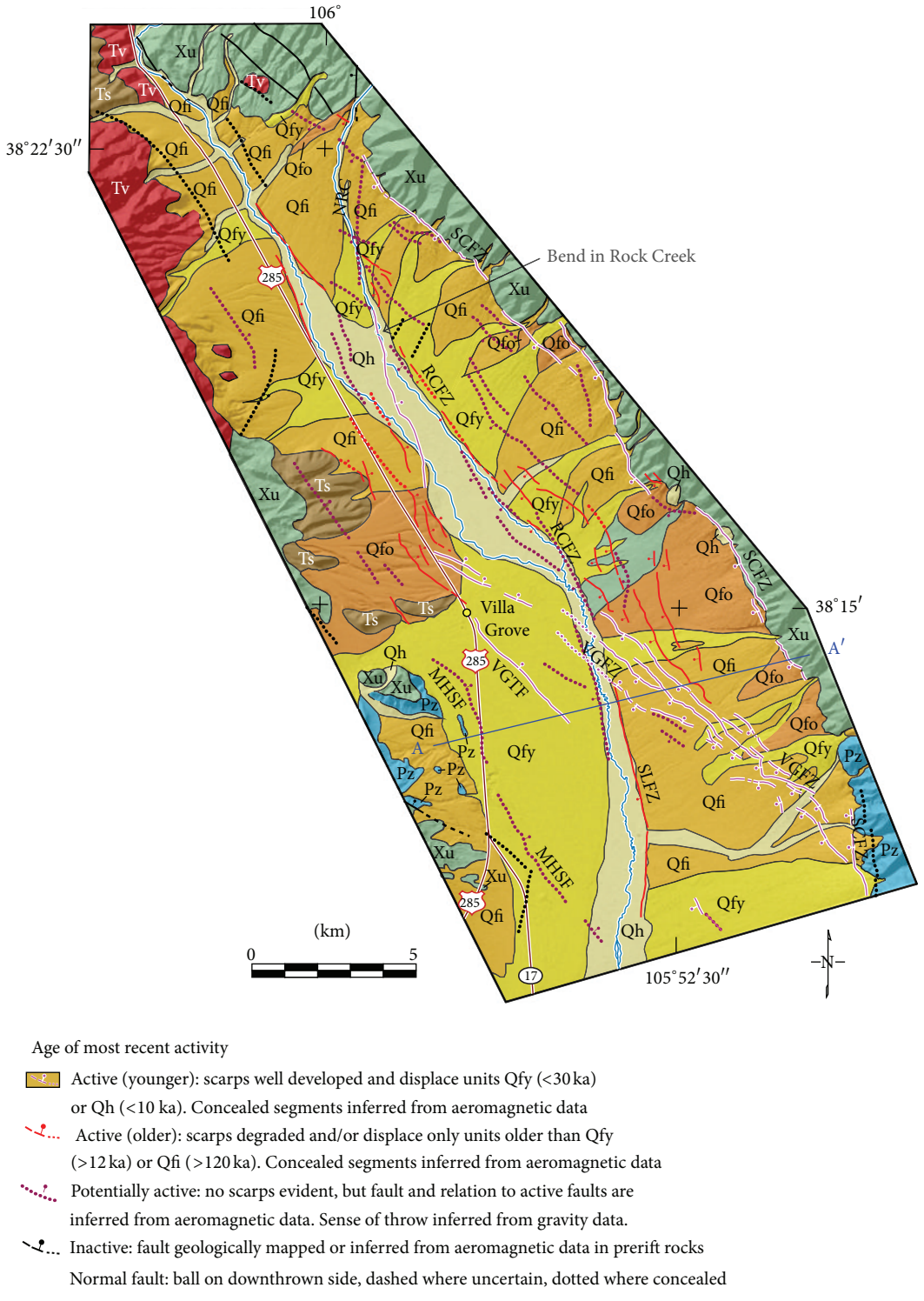

Age of most recent activity

Active (younger): scarps well developed and displace units Qfy (<30 ka) or Qh (<10 ka). Concealed segments inferred from aeromagnetic data

Active (older): scarps degraded and/or displace only units older than Qfy (>12 ka) or Qfi (>120 ka). Concealed segments inferred from aeromagnetic data

Potentially active: no scarps evident, but fault and relation to active faults are inferred from aeromagnetic data. Sense of throw inferred from gravity data.

Inactive: fault geologically mapped or inferred from aeromagnetic data in prerift rocks

Normal fault: ball on downthrown side, dashed where uncertain, dotted where concealed

Figure 15: Revised surficial geology and inferred active faults and buried fault segments resulting from combined interpretation of the aeromagnetic and LiDAR data for the study area. MHSF: Mineral Hot Springs fault (revised), NRC: Northern Rock Creek; RCFZ: Rock Creek fault zone, SCFZ: Sangre de Cristo fault zone, SLFZ: San Luis Creek fault zone, VGFZ: Villa Grove fault zone, and VGTF: Villa Grove town fault. Model for A-A′ is shown in Figure 16.

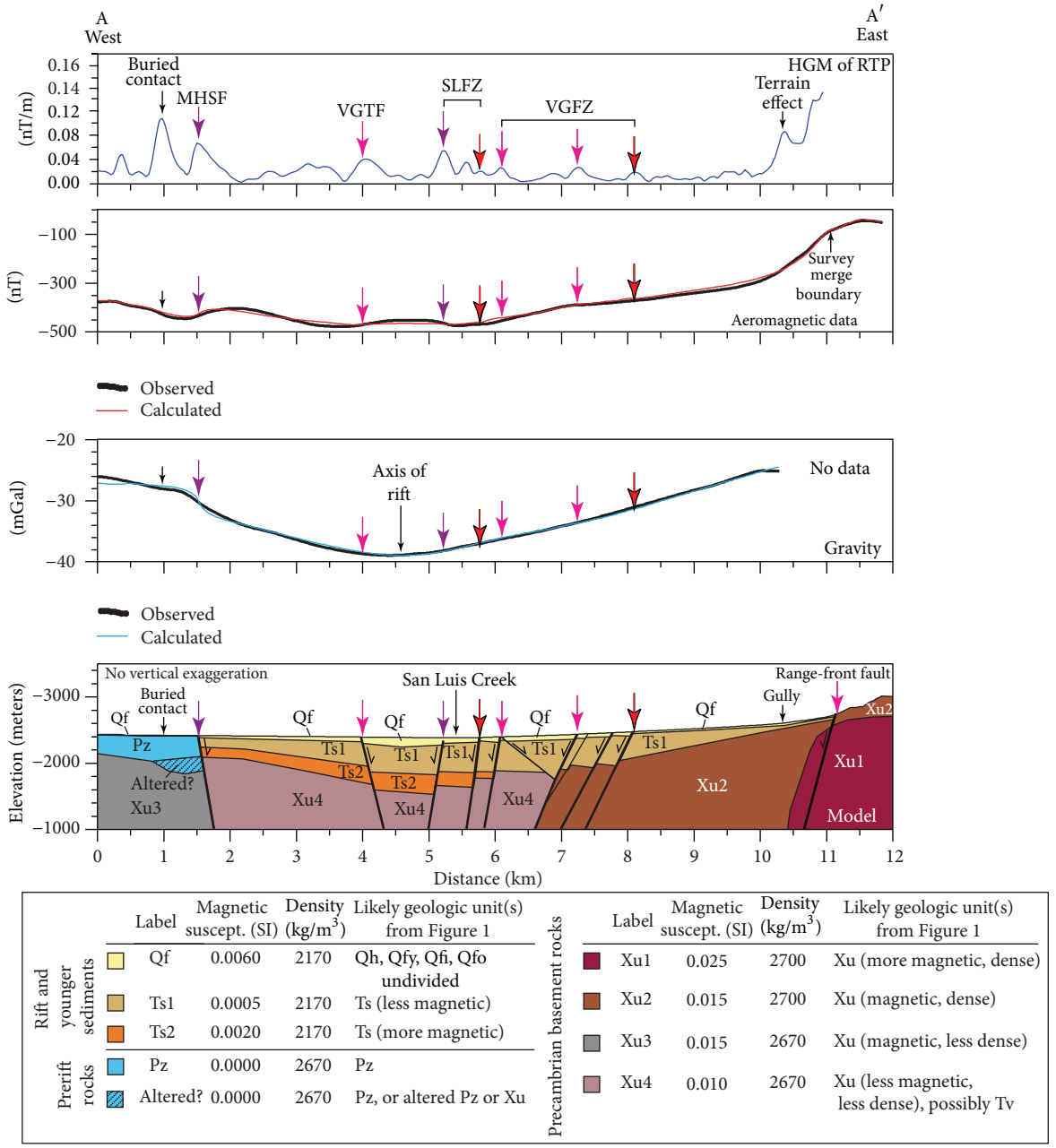

Figure 16: 2D geophysical model for profile A-A′ (located in Figures 2–4, 6, and 15). Observed curves were extracted from the grids for reduced-to-pole aeromagnetic data (Figure 2), isostatic residual gravity (Figure 4), and HGM of the reduced-to-pole aeromagnetic data (HGM of RTP) (Figure 6). MHSF: Mineral Hot Springs fault (revised), SLFZ: San Luis Creek fault zone, VGFZ: Villa Grove fault zone, and VGTF: Villa Grove town fault. Colored arrows point to the locations of inferred faults from Figure 15, coded in a similar fashion: magenta indicates active (younger), red (with black outline) active (older), and purple potentially active.

of gravity values across the Villa Grove fault zone. These relations support geologic evidence that the Villa Grove fault zone represents a wide zone of small displacement faults, primarily down to the southwest along the eastern margin of the rift [8, 10, 21].

7.2. Fault Patterns in the Valley. The HGM ridges from the aeromagnetic data prominently define faults that closely follow creeks in the valley (Figure 6), confirming previous speculation that steep banks along the eastern sides of Rock Creek and San Luis Creek are tectonic rather than fluvial in origin [10]. In addition to the arguments presented for a tectonic origin in regards to example Area 2, further evidence is provided by the linearity of HGM ridges in other parts of the study area that traverse subdued sections of the stream bank, or entirely underlie the creek itself, as demonstrated north of the confluence of San Luis and Rock Creeks (Figure 6). Thus, we use both the LiDAR and aeromagnetic

data together to define the generally north-south San Luis Creek fault zone south of the Villa Grove fault zone, and the northwest-striking Rock Creek fault zone to the north, following Rock Creek upstream to where it bends as it flows from the mountains into the main stream valley (Figure 15).

The Villa Grove town fault should not be considered part of the Villa Grove fault zone, despite previous compilations that list them together (e.g., [8]). A strong signal in the aeromagnetic data (including a strong HGM peak) suggests it has larger displacement than do faults of the Villa Grove fault zone (Figures 2, 6, 12, and 16). Its northeast dip and location on the west side of the gravity low suggest it is part of the western margin of the rift basin (Figure 16). The San Luis Creek fault zone displays multiple splays where it is intersected obliquely by the Villa Grove fault zone and is offset by it (Figure 12), making the San Luis Creek fault an older active system at the eastern margin of the rift basin. It has larger displacement of sediments than the Villa Grove fault zone (as evidenced by stronger aeromagnetic signal), but has little effect on the gravity profile (Figure 16), suggesting that displacement on prerift bedrock associated with these faults is accommodated across multiple faults rather than on one master fault. On the other hand, the western rift margin appears to be focused at the revised Mineral Hot Springs fault (MHSF) (Figure 16). It is associated with a significant drop in gravity values, which signifies a normal offset of Paleozoic and Proterozoic rocks exposed on the west into the rift basin on the east. Decreases in both magnetic and gravity values just west of the Mineral Hot Springs fault were difficult to model geologically. Altered rock that has lost its magnetization is one possible explanation and is compatible with possible explanations for the aeromagnetic low over the hot springs west of the fault to the south (Figure 13).

Fault patterns that generally outline and follow gradients that define gravity lows in the study area support the use of the lows as proxies for defining the shapes of the rift basin (Figure 17). For example, the Villa Grove town fault (VGTF) and the Rock Creek fault zone (RCFZ) nicely outline the eastern and western sides of the gravity low in the center of the study area. The narrowing of this gravity low where it is crossed by profile A-A′ before it widens and deepens to the south appears to be controlled by the Villa Grove fault zone (VGFZ). The Villa Grove fault zone also follows the northwest-southeast trend of the broader flanks of the southern gravity low to the intersection with the Sangre de Cristo fault at the southeastern corner of the study area. The widely distributed, small displacement of the faults of the Villa Grove fault zone may explain why its northwestern extension does not appear to affect the shape of the gravity low as it traverses obliquely to meet the northern part of the Villa Grove town fault. However, this northwestward extension parallels the broad bend in San Luis Creek north of the town of Villa Grove that in turn follows the curve of a broad gradient in the aeromagnetic data (Figure 2). The broad aeromagnetic gradient is indicative of large-volume magnetic sources, such as the juxtaposition of underlying Proterozoic and Paleozoic rocks. The similarities between the stream, Quaternary faults, and broad patterns in the aeromagnetic data suggest that the configuration of prerift rocks may have had some influence on the structural patterns.

Whereas the Rock Creek fault zone (RCFZ) follows the eastern margin of the gravity low, the San Luis Creek fault zone (SLFZ) enigmatically traverses across the deepest part of the southern gravity low, apparently crossing the middle of the rift basin rather than following its border. This relation suggests several possibilities: (1) the rift basin was primarily shaped by early rift activity, (2) the gravity low is partially reflecting underlying thickening of Paleozoic rocks, or (3) prerift structure influenced the subsequent location of the fault and the creek. For the first possibility, perhaps the San Luis Creek fault zone originally connected to the revised Mineral Hot Springs fault on the south, forming the tips of an older half graben that has since been widened by the activity on the Villa Grove fault zone. However, contribution to the gravity low from a greater thickness of Paleozoic rocks in this area is also a distinct possibility, as suggested by seismic-reflection sections across the central part of the gravity low [45]. Evaluation of these possibilities is part of future modeling efforts.

7.3. Prerift Structure or Active Fault? The Rock Creek fault zone is intersected at its northern end, at the bend in the creek, by a younger active fault that traverses obliquely across the valley from the west side of San Luis Creek (Figure 15). The younger active fault (A on Figure 8) aligns with the north-northeast orientation of northern Rock Creek (NRC) in the northeast part of the study area (Figure 15). A prominent north-south aeromagnetic anomaly emanating from the range front follows the northern part of Rock Creek (Figure 2). The magnetic source of the anomaly appears to be fault bounded on its eastern side along a north-south linear gradient and faulted along its southern tip, because the anomaly appears terminated. Although the source of this anomaly likely arises from the Proterozoic basement and some of the faulting may be related to the prerift Laramide orogeny, its alignment with an active younger fault suggests it may have a role in active rifting. Several other enigmatic, northeast-trending linear anomalies that abut the range front obliquely on Figure 2 are also likely related to prerift, probably Laramide, structures. However, they appear to be inactive. Alternatively, these anomalies may arise from dikes present within the bedrock. The presence of dikes intruding rift sediments is unlikely because no magmatism subsequent to the prerift San Juan volcanic field has been recognized in the study area (Figure 1).

7.4. Rift Evolution. Implications for the evolution of the Rio Grande rift in the study area are newly apparent from the faults inferred from the combined interpretation (Figure 15). Potentially active faults are considered the oldest and follow northwest trends on either side of the valley. Faults that have apparently not been active since 120 ka (older active faults) are concentrated in the central part of the valley, and they are crossed by faults with more recent activity (younger active faults). An east-migrating sequence of ages is represented in the example for Area 1 (Figure 8), which is not depicted in the generalized age classification of Figure 15: age constraints

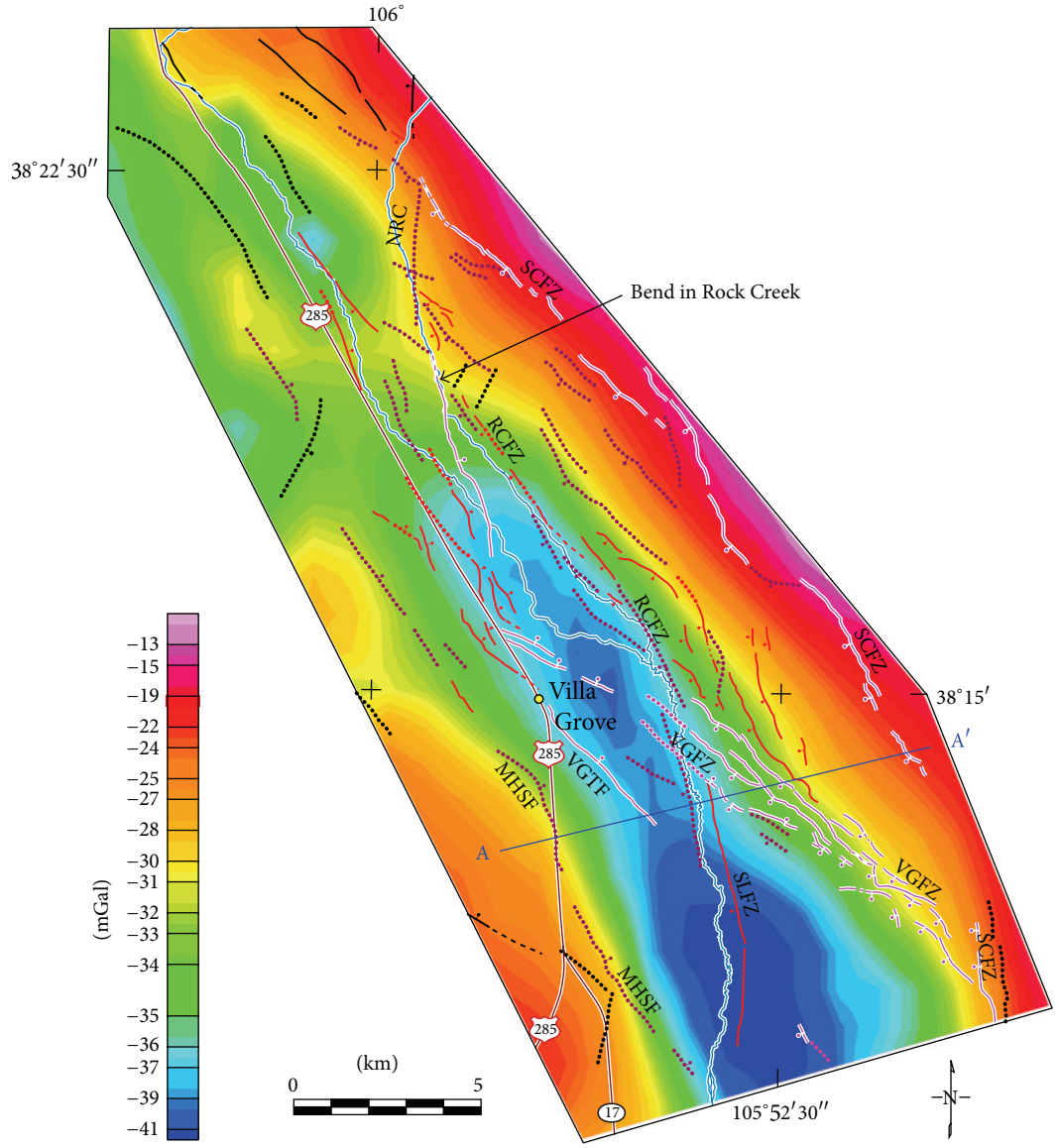

FIGURE 17: Active faults of Figure 15 overlain on the gravity data of Figure 4, a proxy for viewing rift basin shape. MHSF: Mineral Hot Springs fault (revised), NRC: Northern Rock Creek, RCFZ: Rock Creek fault zone, SCFZ: Sangre de Cristo fault zone, SLFZ: San Luis Creek fault zone, VGFZ: Villa Grove fault zone, and VGTF: Villa Grove town fault. Model for A-A′ is shown in Figure 16.

suggest the most recently active fault was on the east side of Area 1 (fault A), preceded by fault B, then C and E (unknown order). Fault D is even older and is classified as potentially active. The oldest interpreted rift fault is concealed, evident from the 2D geophysical model for Area 1 between B and C (Figure 9).

Most recent ruptures on the younger active faults were concentrated on the Sangre de Cristo and Villa Grove fault zones. Although these faults record the most recent ruptures (<30 ka), multiple events recorded on both fault zones suggest they have been active since ~400 ka [5]. Overall, the fault patterns, even those with most recent activity, show an influence from older structure, yet to be fully understood.

8. Conclusions

Combined interpretation of aeromagnetic and LiDAR data builds on the strength of the aeromagnetic method to locate normal faults with significant offset under cover and the strength of using LiDAR images to identify the age and sense of motion of faults. Each dataset helps resolve ambiguities in interpreting the other. In addition, gravity data can be used to infer the sense of motion for totally buried faults inferred solely from aeromagnetic data.

The most common benefits from combining the methods are as follows:

(i) results from aeromagnetic interpretation help guide the proper connection of fault traces between

discontinuous scarps apparent in the LiDAR data and help resolve tectonic versus fluvial origin for topographic scarps next to streams;

(ii) results from LiDAR interpretation help locate the surface fault trace from multiple or ambiguous peaks in aeromagnetic gradient data;

(iii) identification of fault scarps from the LiDAR data provide evidence that an inferred fault is active;

(iv) orientations of fault scarp faces from the LiDAR data suggest the sense of displacement for inferred faults;

(v) patterns of active rift faults or locations of basin margins determined from gravity data provide guidance for determining the relative age of completely buried, aeromagnetically inferred faults from their locations and strike directions.

Combined interpretation to identify active faults in the northern San Luis Basin of the northern Rio Grande rift has confirmed general aspects of previous geologic mapping but has also provided significant improvements. The interpretation revises and extends mapped fault traces, confirms tectonic versus fluvial origins of steep stream banks, and gains additional information on the nature of active and potentially active partially and totally buried faults. In general, tectonics appears to have a large control on the geomorphology. Tectonic activity was concentrated in the central part of the valley throughout most of rift history. Activity at the range front began fairly late and has produced little displacement so far (~100 m).

Detailed morphology of surfaces mapped from the LiDAR data helps constrain ages of the faults that displace the deposits. The aeromagnetic data provide additional information about their extents in between discontinuous fault scarps and suggest several totally buried, potentially active faults are present on both sides of the valley, surrounding gravity lows that likely represent the shape of the rift basin. An enigmatic linear aeromagnetic anomaly in line with a younger active fault suggests that prerift structure may have a role in rifting.

Acknowledgments

The authors are grateful to Ted Brandt (USGS) who developed the LiDAR images and Ben Drenth (USGS) who prepared the gravity data and shared his preliminary modeling with them. They appreciate reviews by Jonathan Glen (USGS) and two journal reviewers, which greatly improved the paper. This project was supported by the National Cooperative Geologic Mapping Program. Aeromagnetic data were partially supported by the Colorado Geological Survey, USGS Geothermal Program, and the Task Force for Stability and Business Operations. LiDAR acquisition was part of a coalition of Federal and State partners, coordinated by Carol Giffin (USGS). Any use of trade, product, or firm names in this publication is for descriptive purposes only and does not imply endorsement by the U.S. Government. Authors have no affiliation with nor financial interest in EONGeosciences company.

References

[1] R. J. Blakely, B. L. Sherrod, J. F. Hughes, M. L. Anderson, R. E. Wells, and C. S. Weaver, "Saddle Mountain fault deformation zone, Olympic Peninsula, Washington: Western boundary of the Seattle uplift," *Geosphere*, vol. 5, no. 2, pp. 105–125, 2009.

[2] R. J. Blakely, B. L. Sherrod, C. S. Weaver et al., "Connecting the Yakima fold and thrust belt to active faults in the Puget Lowland, Washington," *Journal of Geophysical Research B*, vol. 116, no. 7, Article ID B07105, 2011.

[3] V. J. S. Grauch and M. R. Hudson, "Guides to understanding the aeromagnetic expression of faults in sedimentary basins: lessons learned from the central Rio Grande Rift, New Mexico," *Geosphere*, vol. 3, no. 6, pp. 596–623, 2007.

[4] R. M. Kirkham and W. P. Rogers, "Earthquake potential in Colorado," Colorado Geological Survey Bulletin 43, 1981, http://geosurvey.state.co.us/pubs/online/Documents/1981%20Bulletin%2043.pdf.

[5] J. P. McCalpin, "Quaternary tectonics of the Sangre de Cristo and Villa Grove fault zones," in *Contributions to Colorado Seismicity and Tectonics, a 1986 Update*, W. P. Rogers and R. M. Kirkham, Eds., Colorado Geological Survey Special Publication 28, pp. 59–64, 1986.

[6] R. M. Kirkham, Compiler, "Fault number 2320, Mineral Hot Springs fault," in *Quaternary fault and fold database of the United States*, U.S. Geological Survey, 1998, http://earthquakes.usgs.gov/regional/qfaults.

[7] R. M. Kirkham, Compiler, "Fault number 2321b, Northern Sangre de Cristo fault, Crestone section," in *Quaternary fault and fold database of the United States*, U.S. Geological Survey, 1998, http://earthquakes.usgs.gov/regional/qfaults.

[8] R. M. Kirkham, Compiler, "Fault number 2319, Villa Grove fault zone," in *Quaternary fault and fold database of the United States*, U.S. Geological Survey, 1998, http://earthquakes.usgs.gov/regional/qfaults.

[9] Colorado Earthquake Hazards Mitigation Council, *Colorado Earthquake Hazards*, Colorado Geological Survey, 2008, http://geosurvey.state.co.us/hazards/Earthquakes/Documents/Earthquake_Map_2008.pdf.

[10] C. Ruleman and M. N. Machette, "An overview of the Sangre de Cristo fault system and new insights to interactions between Quaternary faults in the northern Rio Grande rift," in *2007 Rocky Mountain Section Friends of the Pleistocene Field Trip—Quaternary Geology of the San Luis Basin of Colorado and New Mexico, September 7–9, 2007*, M. N. Machette, M. M. Coates, and M. L. Johnson, Eds., U.S. Geological Survey Open-File Report 2007-1193, pp. 187–197, 2007, http://pubs.usgs.gov/of/2007/1193/pdf/OF07-1193_ChJ.pdf.

[11] G. R. Keller and W. S. Baldridge, "The Rio Grande rift: a geological and geophysical overview," *Rocky Mountain Geology*, vol. 34, no. 1, pp. 121–130, 1999.

[12] C. F. Kluth and C. H. Schaftenaar, "Depth and geometry of the northern Rio Grande rift in the San Luis Basin, south-central Colorado," in *Basins of the Rio Grande Rift: Structure, Stratigraphy, and Tectonic Setting*, G. R. Keller and S. M. Cather, Eds., Geological Society of America Special Paper 291, pp. 27–37, 1994.

[13] D. A. Lindsey, R. F. Clark, and S. J. Soulliere, "Minturn and Sangre de Cristo Formations of southern Colorado: a prograding fan delta and alluvial fan sequence shed from the Ancestral Rocky Mountains," in *Paleotectonics and Sedimentation*, J. A. Peterson, Ed., American Association of Petroleum Geologists Memoir 41, pp. 541–561, 1986.

[14] D. A. Lindsey, B. R. Johnson, and P. A. M. Andriessen, "Laramide and Neogene structure of the northern Sangre de Cristo Range, South-Central Colorado," in *Rocky Mountain Foreland Basins and Uplifts*, J. D. Lowell, Ed., pp. 219–228, Rocky Mountain Association of Geologists, Denver, Colo, USA, 1983.

[15] B. S. Brister and R. R. Gries, "Tertiary stratigraphy and tectonic development of the Alamosa basin (northern San Luis Basin), Rio Grande rift, south-central Colorado," in *Basins of the Rio Grande Rift: Structure, Stratigraphy, and Tectonic Setting*, G. R. Keller and S. M. Cather, Eds., Geological Society of America Special Paper 291, pp. 39–58, 1994.

[16] R. J. Varga and B. M. Smith, "Evolution of the early Oligocene Bonanza caldera, northeast San Juan volcanic field, Colorado," *Journal of Geophysical Research*, vol. 89, no. 10, pp. 8679–8694, 1984.

[17] P. W. Lipman and W. C. McIntosh, "Erosionally exhumed fill and floor of a ring-fault-bounded plate-subsidence caldera: 33. 2-Ma Bonanza, Southwest Colorado," *Eos Transactions of the American Geophysical Union*, vol. 90, no. 52, 2009, Fall Meeting Supplement, Abstract V23C-2080.

[18] R. A. Thompson, C. M. Johnson, and H. H. Mehnert, "Oligocene basaltic volcanism of the northern Rio Grande Rift: San Luis Hills, Colorado," *Journal of Geophysical Research*, vol. 96, no. 8, pp. 13577–13592, 1991.

[19] C. E. Chapin and S. Cather, "Tectonic setting of the axial basins of the northern and central Rio Grande rift," in *Basins of the Rio Grande Rift: Structure, Stratigraphy, and Tectonic Setting*, G. R. Keller and S. M. Cather, Eds., Geological Society of America Special Paper 291, pp. 5–23, 1994.

[20] H. T. Berglund, A. F. Sheehan, M. H. Murray et al., "Distributed deformation across the Rio Grande Rift, Great Plains, and Colorado Plateau," *Geology*, vol. 40, no. 1, pp. 23–26, 2012.

[21] J. McCalpin, "Quaternary geology and neotectonics of the west flank of the Northern Sangre de Cristo Mountains, South-Central Colorado," *Colorado School of Mines Quarterly*, vol. 77, no. 3, p. 97, 1982.

[22] J. R. Shannon and J. P. McCalpin, "Geologic map of the Maysville quadrangle, Chaffee County, Colorado," Colorado Geological Survey Open-File Report 06-10, 2009, http://geosurveystore.state.co.us/p-935-maysville-quadrangle-chaffee-county-colorado.aspx.

[23] O. Tweto, "The Rio Grande rift system in Colorado," in *Rio Grande Rift: Tectonics and Magmatism*, R. E. Riecker, Ed., pp. 33–56, American Geophysical Union, Washington, DC, USA, 1979.

[24] S. M. Colman, J. P. McCalpin, D. A. Ostenaa, and R. M. Kirkham, "Map showing upper Cenozoic rocks and deposits and Quaternary faults, Rio Grande rift, South-Central Colorado," U.S. Geological Survey Miscellaneous Investigations Map I-1594, 2 sheets, scale 1:125, 000, 1985, http://pubs.er.usgs.gov/publication/i1594.

[25] M. N. Machette, R. A. Thompson, and B. J. Drenth, "Geologic map of the San Luis quadrangle, Costilla County, Colorado," U.S. Geological Survey Scientific Investigations Map 2963, 1 sheet, scale 1:24, 000, 2008, http://pubs.usgs.gov/sim/2963/.

[26] K. A. Brugger, "Cosmogenic ^{10}Be and ^{36}Cl ages from Late Pleistocene terminal moraine complexes in the Taylor River drainage basin, central Colorado, USA," *Quaternary Science Reviews*, vol. 26, no. 3-4, pp. 494–499, 2007.

[27] K. S. Kellogg, R. R. Shroba, B. Bryant, and W. R. Premo, "Geologic map of the Denver West 30′ x 60′ quadrangle, north-central Colorado," U.S. Geological Survey Scientific Investigations Map 3000, 2008, http://pubs.usgs.gov/sim/3000/.

[28] J. P. Briner, "Moraine pebbles and boulders yield indistinguishable ^{10}Be ages: a case study from Colorado, USA," *Quaternary Geochronology*, vol. 4, no. 4, pp. 299–305, 2009.

[29] C. A. Ruleman, R. G. Bohannon, B. Bryant, R. R. Shroba, and W. R. Premo, "Geologic map of the Bailey 30′ x 60′ Quadrangle, Colorado," U.S. Geological Survey Scientific Investigations Map 3156, scale 1:100, 000, 2011, http://pubs.usgs.gov/sim/3156/.

[30] N. E. Young, J. P. Briner, E. M. Leonard, J. M. Licciardi, and K. Lee, "Assessing climatic and nonclimatic forcing of Pinedale glaciation and deglaciation in the western United States," *Geology*, vol. 39, no. 2, pp. 171–174, 2011.

[31] C. A. Ruleman, R. A. Thompson, R. R. Shroba et al., "Late Miocene-Pleistocene evolution of a Rio Grande rift subbasin, Sunshine Valley-Costilla Plain, San Luis Basin, New Mexico and Colorado," in *New Perspectives on Basins of the Rio Grande Rift: From Tectonics to Groundwater*, M. R. Hudson and V. J. S. Grauch, Eds., Geological Society of America Special Paper 494, pp. 47–73, 2013.

[32] K. S. Kellogg, "Neogene basins of the northern Rio Grande rift: partitioning and asymmetry inherited from Laramide and older uplifts," *Tectonophysics*, vol. 305, no. 1–3, pp. 141–152, 1999.

[33] D. H. Knepper Jr., *Tectonic analysis of the Rio Grande rift zone, central Colorado [Ph.D. thesis]*, Colorado School of Mines, Golden, Colo, USA, 1974.

[34] D. A. Lindsey and S. J. Soulliere, "Geologic map and sections of the Valley View Hot Springs Quadrangle, Custer and Saguache counties, Colorado," U.S. Geological Survey Miscellaneous Field Studies Map, MF-1942, scale 1:24, 000, 1987.

[35] G. R. Scott, R. B. Taylor, R. C. Epis, and R. A. Wobus, "Geologic map of the Pueblo 1 x 2 quadrangle, South-Central Colorado," U.S. Geological Survey Miscellaneous Investigations Map I-1022, scale 1:250, 000, 1978, http://pubs.er.usgs.gov/publication/i1022.

[36] R. E. Van Alstine, "Geologic map of the Bonanza NE quadrangle, Chaffee and Saguache Counties, Colorado," U.S. Geological Survey Open-File Report 75-53, scale 1:62, 500, 1975, http://ngmdb.usgs.gov/ngm-bin/ILView.pl?sid=15201_1.sid&vtype=b&sfact=1.5.

[37] J. A. Cappa and C. A. Wallace, "Saguache county, geology and mineral resources," Colorado Geological Survey Resource Series 44, CD-ROM, 2007, http://geosurveystore.state.co.us/p-1026-saguache-county-geology-and-mineral-resources.aspx.

[38] C. C. Finlay, S. Maus, C. D. Beggan et al., "International geomagnetic reference field: the eleventh generation," *Geophysical Journal International*, vol. 183, no. 3, pp. 1216–1230, 2010.

[39] U. S. Geological Survey and National Geophysical Data Center, "Digital aeromagnetic datasets for the conterminous United States and Hawaii—a companion to the North American magnetic anomaly map," U.S. Geological Survey Open-File Report 02-361, version 1. 0, project 4068, 2002, http://pubs.usgs.gov/of/2002/ofr-02-361/.

[40] J. E. Case and R. F. Sikora, "Geologic interpretation of gravity and magnetic data in the Salida region, Colorado," U.S. Geological Survey Open-File Report 84-372, 1984, http://pubs.usgs.gov/of/1984/0372/report.pdf.

[41] Pan-American Center for Earth and Environmental Studies (PACES), "Gravity data portal for the United States," University

of Texas, El Paso, Tex, USA, 2009, http://irpsrvgis00.utep.edu/repositorywebsite/.

[42] C. E. Heywood, "Isostatic residual gravity anomalies of New Mexico," U. S. Geological Survey, Water-Resources Investigations Report 91-4065, 1992, http://pubs.er.usgs.gov/publication/wri914065.

[43] V. J. S. Grauch and S. D. Connell, "New perspectives on the geometry of the Albuquerque Basin, Rio Grande Rift, New Mexico—insights from geophysical models of rift-fill thickness," in *New Perspectives on Rio Grande Rift Basins: From Tectonics to Groundwater*, M. R. Hudson and V. J. S. Grauch, Eds., Geological Society of America Special Paper 494, pp. 427–462, 2013.

[44] D. Stoughton, *Interpretation of seismic reflection data from the San Luis Valley, south-central Colorado [Unpublished PhD thesis T-1960]*, Colorado School of Mines, Golden, Colo, USA, 1977.

[45] T. L. Davis and D. Stoughton, "Interpretation of seismic reflection data from the northern San Luis Valley, South-Central Colorado," in *Rio Grande Rift: Tectonics and Magmatism*, R. E. Riecker, Ed., pp. 185–194, American Geophysical Union, Washington, DC, USA, 1979.

[46] M. R. Hudson, V. J. S. Grauch, and S. A. Minor, "Rock magnetic characterization of faulted sediments with associated magnetic anomalies in the Albuquerque Basin, Rio Grande rift, New Mexico," *Geological Society of America Bulletin*, vol. 120, no. 5-6, pp. 641–658, 2008.

[47] V. J. S. Grauch and M. R. Hudson, "Aeromagnetic anomalies over faulted strata," *The Leading Edge*, vol. 30, no. 11, pp. 1242–1252, 2011.

[48] L. Cordell and V. J. S. Grauch, "Mapping basement magnetization zones from aeromagnetic data in the San Juan Basin, New Mexico," in *The Utility of Regional Gravity and Magnetic Anomaly Maps*, W. J. Hinze, Ed., pp. 181–197, Society of Exploration Geophysicists, Tulsa, Okla, USA, 1985.

[49] R. J. Blakely and R. W. Simpson, "Approximating edges of source bodies from magnetic or gravity anomalies," *Geophysics*, vol. 51, no. 7, pp. 1494–1498, 1986.

[50] V. J. S. Grauch and C. S. Johnston, "Gradient window method: a simple way to separate regional from local horizontal gradients in gridded potential-field data," *Society of Exploration Geophysicists Technical Program Expanded Abstracts*, pp. 762–765, 2002.

[51] R. C. Bucknam and R. E. Anderson, "Estimation of fault-scarp ages from scarp height-slope-angle relationships," *Geology*, vol. 7, pp. 11–14, 1979.

[52] M. N. Machette, "Contrasts between short- and long-term records of seismicity in the Rio Grande rift—important implications for seismic hazard assessments in areas of slow extension," in *Western States Seismic Policy Council Proceedings Volume, Basin and Range Province Seismic Hazards Summit*, W. R. Lund, Ed., Utah Geological Survey Miscellaneous Publication 98–2, pp. 84–95, Utah Geological Survey, 1998.

[53] A. Valdez, "Stop A8—closed basin overflow and origin of Hansen Bluff," in *2007 Rocky Mountain Section Friends of the Pleistocene Field Trip—Quaternary Geology of the San Luis Basin of Colorado and New Mexico, September 7–9, 2007*, M. N. Machette, M. M. Coates, and M. L. Johnson, Eds., U.S. Geological Survey Open-File Report 2007-1193, pp. 38–39, 2007, http://pubs.usgs.gov/of/2007/1193/pdf/OF07-1193_ChA.pdf.

[54] W. B. Bull, "The alluvial fan environment," *Progress in Physical Geography*, vol. 1, no. 2, pp. 222–270, 1977.

[55] O. Tweto and J. E. Case, *Gravity and Magnetic Features As Related to Geology in the Leadville 30-Minute Quadrangle, Colorado*, U.S. Geological Survey Professional Paper 726-C, 1972.

[56] J. D. Phillips, R. O. Hansen, and R. J. Blakely, "The use of curvature in potential-field interpretation," *Exploration Geophysics*, vol. 38, no. 2, pp. 111–119, 2007.

[57] B. R. Johnson, D. A. Lindsey, R. M. Bruce, and S. J. Soulliere, "Reconnaissance geologic map of the Sangre de Cristo Wilderness Study Area, South-Central Colorado," U.S. Geological Survey Miscellaneous Field Studies Map MF-1635-B, scale 1:62, 500, 1987.